Depletion of CD206^{+} Tumour Macrophages via a Peptide-Targeted Star-Shaped Polyglutamate Inhibits Tumourigenesis and Metastatic Dissemination in Mouse Breast Cancer Models

Anni Lepland[¥,1], Alessio Malfanti[¥,2], Uku Haljasorg[3], Eliana K. Asciutto[4], Monica Pickholz[5,6], Mauro Bringas[7,8], Snežana Đorđević[2], Liis Salumäe[9], Pärt Peterson[3], Tambet Teesalu[ψ,1,10], María J. Vicent[ψ,2], Pablo Scodeller[ψ,1]

¥: equal contribution
ψ: equal contribution

[1] Laboratory of Precision and Nanomedicine, Institute of Biomedicine and Translational Medicine, University of Tartu, Ravila 14B, Tartu, 50411, Estonia

[2] Polymer Therapeutics Laboratory, Prince Felipe Research Centre, Av. Eduardo Primo Yúfera 3, Valencia 46012, Spain

[3] Molecular Pathology Research Group, Institute of Biomedicine and Translational Medicine, University of Tartu, Ravila 19, Tartu, 50412, Estonia

[4] School of Science and Technology, National University of San Martin (UNSAM) ICIFI and CONICET. Buenos Aires, Argentina.

[5] Departamento de Física, Facultad de Ciencias Exactas y Naturales, Universidad de Buenos Aires, Buenos Aires

[6] Instituto de Física de Buenos Aires (IFIBA), CONICET-Universidad de Buenos Aires, Buenos Aires, Argentina

[7] Departamento de Química Inorgánica, Analítica y Química Física, Facultad de Ciencias Exactas y Naturales, Universidad de Buenos Aires, Ciudad de Buenos Aires, C1428EHA, Argentina

[8] Fundación Instituto Leloir, Instituto de Investigaciones Bioquímicas de Buenos Aires (IIBBA-CONICET), C1405BWE Ciudad Autónoma de Buenos Aires, Buenos Aires, Argentina.

[9] Tartu University Hospital, Pathology department, Puusepa 8, 50406, Estonia

[10] Centre for Nanomedicine and Department of Cell, Molecular and Developmental Biology, University of California, Santa Barbara, 93106, CA, USA

ABSTRACT

Although many studies have explored the depletion of tumour-associated macrophages (TAMs) as a therapeutic strategy for solid tumours, currently available compounds suffer from poor efficacy and dose-limiting side effects. Here, we developed a novel TAM-depleting agent ("OximUNO") that specifically targets CD206$^+$ TAMs and demonstrated efficacy in triple negative breast cancer (TNBC) mouse models. OximUNO comprises a star-shaped polyglutamate (St-PGA) decorated with the CD206-targeting peptide mUNO that carries the chemotherapeutic drug doxorubicin (DOX). In TNBC models, a fluorescently-labelled mUNO-decorated St-PGA homed to CD206$^+$ TAMs within primary lesions and metastases. OximUNO exhibited no acute liver or kidney toxicity in vivo. Treatment with OximUNO reduced the progression of primary tumour lesions and pulmonary metastases, significantly diminished the number of CD206$^+$ TAMs and increased the CD8/FOXP3 expression ratio (demonstrating immunostimulation). Our findings suggest the potential benefit of OximUNO as a TAM-depleting agent for TNBC treatment. Importantly, our studies also represent the first report of a peptide-targeted St-PGA as a targeted therapeutic nanoconjugate.

Keywords: polymer-drug nanoconjugates, targeting peptide, CD206, tumour-associated macrophages, triple negative breast cancer, pulmonary metastasis, immunomodulation

INTRODUCTION

Triple negative breast cancer (TNBC), defined by the lack of the expression of the oestrogen receptor (ER), progesterone receptor (PR), and human epidermal growth factor receptor 2 (HER2)[1,2], represents an aggressive breast cancer subtype with poor prognosis[3] that comprises up to 20% of all breast cancer cases[3,4]. Interfering with immune checkpoints signalling (e.g. through the modulation of programmed cell death 1 (PD-1) and its ligand (PD-L1)) represents an alternative treatment strategy for several cancers and is currently being employed in combination with chemotherapy as a neoadjuvant or adjuvant treatment[5–8]. The U.S. Food and Drug Administration (FDA) recently granted accelerated approval for a combination of a PD-L1 blocking antibody (atezolizumab, Tecentriq®) and nab-paclitaxel (Abraxane®)[9] as a first-line treatment for unresectable locally advanced or metastatic TNBC[10]. While promising clinical results have resulted, this combinatorial treatment approach suffers from significant obstacles, including the problematic identification and heterogeneity of PD-L1 expression in

70 patients[11], the limited applicability to PD-L1 positive TNBC patients (only 20–42% of
71 cases)[12,13], and the induction of severe side effects (e.g., neutropenia, peripheral neuropathy,
72 and colitis)[10,14,15]. Other immune checkpoint inhibitors (ICIs), including the cytotoxic T
73 lymphocyte-associated antigen 4 (CTLA-4) blockers ipilimumab and tremelimumab, are
74 currently under evaluation for TNBC treatment in combination with other drugs (clinical trial
75 identifiers: NCT03606967, NCT02983045); however, anti-CTLA-4 treatments induce severe
76 side effects such as endocrinopathies, myopathy, enterocolitis, and hepatitis[16–19], which narrow
77 their use. Overall, the limited success of alternative treatment options for TNBC has maintained
78 chemotherapy as the standard of care for most patients[20].
79 The anthracycline drug doxorubicin (DOX), which presents high off-target effects such as
80 cardiotoxicity[21,22], represents a frequently employed chemotherapeutic for TNBC; however,
81 disease relapse and metastatic development have also been associated with DOX treatment[23].
82 M2 (anti-inflammatory)-polarised tumour-associated macrophages (TAMs)[24] found within
83 both primary and metastatic tumour lesions mediate both events[25]; furthermore, TAMs
84 represent the main executioners of tumour progression, immunosuppression and invasion[24–29],
85 and their presence correlates with inadequate therapeutic response and poor prognosis[25].
86 Recent efforts have focused on eliminating TAMs, and several ongoing clinical trials are
87 currently evaluating TAM depletion in combination with treatments such as ICIs[30]. The current
88 clinical-stage gold standard for TAM depletion relies on agents that block colony stimulating
89 factor 1 (CSF1) or its receptor CSF1R, such as the small molecule CSF1R inhibitor PLX3397[31];
90 however, microglia also expresses CSF1R[32], the inhibition of CSF1R with PLX5622 impacts
91 M1 macrophages[33], and PLX3397 treatment causes oedema[34]. Clinical data suggests that anti-
92 CSF1R antibodies induce a modest effect[35,36] and cause severe side effects that include
93 haematological toxicities[35] and hepatotoxicity by targeting Kupfer cells[35,36]. Overall, these
94 findings highlight the overwhelming need for new TAM-depletion strategies.
95 Notably, both perivascular TAMs associated with disease relapse and therapeutic resistance[24]
96 and metastasis-associated macrophages[37] express the mannose receptor (CD206/MRC1).
97 Perivascular TAMs employ CD206 to navigate the surrounding collagen-dense stroma[38],
98 which favours tumour progression[39,40].
99 For the first time, we report the effects of depleting the $CD206^+$ subpopulation of TAMs in
100 metastatic TNBC mouse models through the use of a targeting agent (the mUNO peptide) for
101 a CD206 site different from the mannose-binding site[41–44]. Previous studies have employed
102 mannose to target CD206; however, mannose has other receptors besides CD206[45,46].

We decorated a three-arm branched biodegradable multivalent polyanion with a defined negative charge and nanometre-size hydrodynamic radius (star-shaped polyglutamate or St-PGA) with mUNO peptide to function as a targeted delivery platform for a chemotherapeutic agent (DOX) conjugated through a bioresponsive linker. St-PGA-DOX-mUNO (referred to as OximUNO) efficiently depleted CD206^{+} TAMs, relieved immunosuppression in the tumour microenvironment (TME) and limited metastasis/tumour growth, thereby supporting OximUNO as an alternative TAM depletion strategy.

Most importantly, this study represents the first described combination of two reported technologies – the St-PGA nanocarrier and the mUNO targeting peptide. Overall, this OximUNO proof-of-concept demonstrates the potential of the peptide-targeted St-PGA nanosystem. Our studies lay a foundation for future work using this nanosystem to target other receptors efficiently by changing the targeting peptide.

RESULTS

Design and structural modelling of St-PGA-OG-mUNO

To characterise and explore the function of OximUNO, we first developed an mUNO-targeted St-PGA labelled with the Oregon Green (OG) fluorescent dye (referred to as St-PGA-OG-mUNO) (Fig. 1A, Scheme S1). We conjugated OG to St-PGA using an amide linker to allow in vitro or in vivo tracking and coupled mUNO through a disulphide bond formed between the free cysteine of mUNO and a pyridyldithiol linker on St-PGA. We previously demonstrated that mUNO conjugated to polymeric nanostructures through the cysteine thiol group preserves CD206 binding[42]. To evaluate the structure and dye loading, we analysed St-PGA-OG-mUNO and St-PGA-OG using nuclear magnetic resonance (NMR) and UV-Vis analyses (Fig. S1).

Dynamic light scattering (DLS) analysis demonstrated that St-PGA-OG-mUNO and St-PGA-OG displayed similar hydrodynamic diameters of 6.8 and 5.9 nm, respectively (Fig. 1B, C), while both nanoconjugates exhibited highly negative charges (-42 mV and -48 mV, respectively) as shown by Zeta potential analysis (Fig. 1B); an expected result given the glutamic acid nature of the polymer carrier. Analysis of mUNO loading (Fig. 1B) indicated the presence of approximately seven mUNO peptides in St-PGA-mUNO nanoconjugate, which would allow multivalent receptor binding.

We next assessed the structure of unlabelled and untargeted St-PGA in water using molecular dynamics (MD) simulations to access information at the atomic scale. We assumed an initial

136 helical conformation for the three PGA chains. The studied system consisted of a fully hydrated
137 St-PGA and the Na^+ counterions (~920,000 atoms) and was built after initial minimisation
138 under vacuum conditions. We simulated 50 ns of the entire St-PGA macromolecule, with Fig.
139 1D displaying a snapshot corresponding to the last step of the simulation. Averaging the
140 gyration radius over the last 25 ns of the simulation run provided a value of 5.6 ± 0.3 nm, which
141 lies in the same order of magnitude as the results from DLS analysis and suggests a lack of
142 aggregation of both St-PGA-OG-mUNO and St-PGA-OG in PBS. A video simulation (Video
143 S1) suggested that the three PGA chains remain in an extended conformation throughout the
144 simulation and do not show any intra- or inter-molecular interaction, suggesting that the mUNO
145 peptides linked to St-PGA will not interfere with each other.
146 To investigate if mUNO can engage with the CD206 receptor when grafted onto St-PGA, we
147 modelled the structure and mobility of St-PGA-mUNO using computational analysis. To attain
148 a computationally feasible system, we simulated only single branches of St-PGA-mUNO. We
149 placed three equidistant mUNO peptides on a PGA single branch and fully solvated the system.
150 We observed that three mUNO peptides remained exposed to the solution available for receptor
151 binding (Fig. 1E). The rotation of mUNO around PGA, tracked by the angle formed by a
152 proline aromatic carbon within mUNO (Fig. S2, green sphere), a pyridyldithiol linker nitrogen
153 (Fig. S2, blue sphere), and a glutamic acid aromatic carbon (Fig. S2, light blue sphere) revealed
154 angles between 50º and 180º (Fig. 1F). This value supports the ability of mUNO peptides to
155 interact with their receptor[43]. Comparisons with an undecorated PGA branch demonstrated the
156 minimal alterations of secondary structure dynamics in the presence of mUNO peptides -
157 turning alpha helices (Fig. 1G, green) into random coils (Fig. 1G, brown) at regions where they
158 are placed; however, the PGA chain structure remained mainly helical except in the middle,
159 where a slight kink formed (Fig. 1G).
160

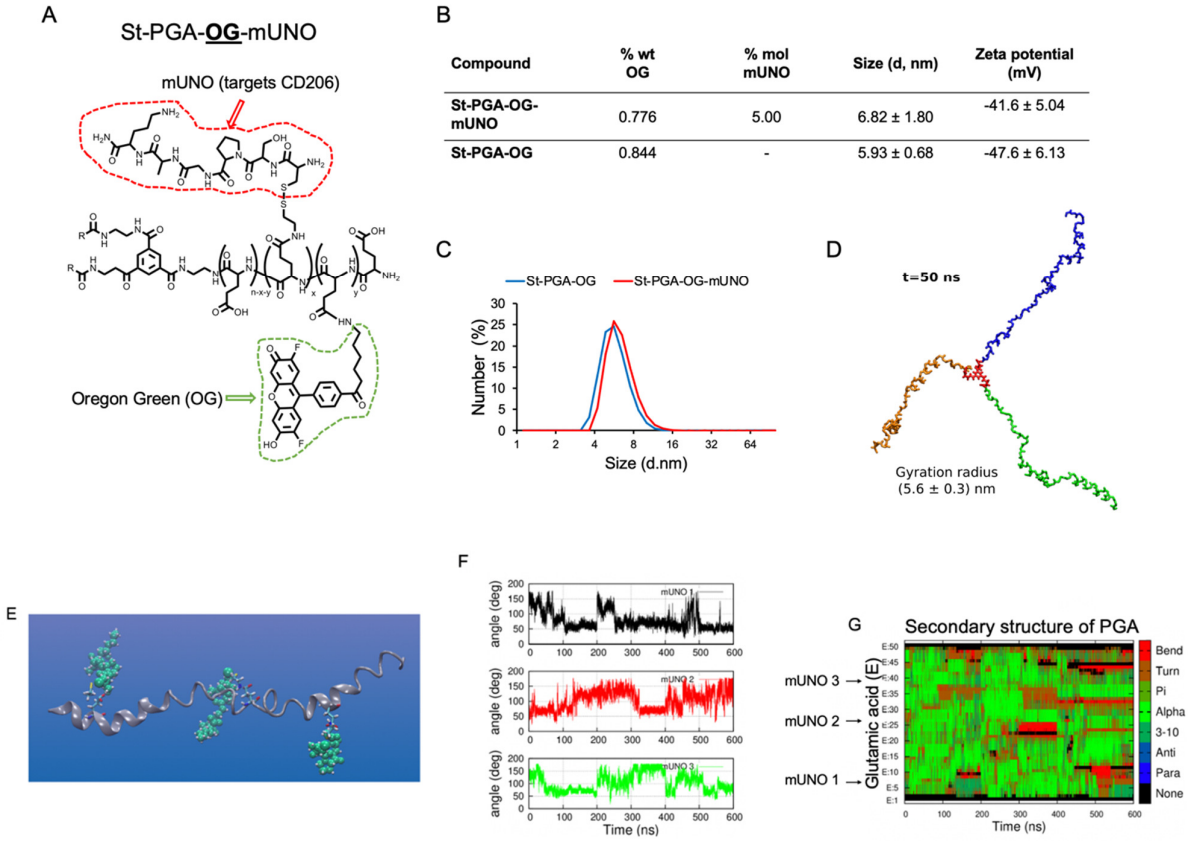

Compound	% wt OG	% mol mUNO	Size (d, nm)	Zeta potential (mV)
St-PGA-OG-mUNO	0.776	5.00	6.82 ± 1.80	-41.6 ± 5.04
St-PGA-OG	0.844	-	5.93 ± 0.68	-47.6 ± 6.13

Figure 1. Design and analysis of mUNO-targeted St-PGA. (**A**) Representative structure of St-PGA decorated with mUNO peptides (red) and OG (green). (**B**) Table detailing OG loading, mUNO loading, size (as measured by DLS), and charge (as measured by Zeta potential analysis). (**C**) DLS graph demonstrating uniform size for both St-PGA-OG-mUNO and St-PGA-OG. (**D**) A snapshot of modelled St-PGA structure in water and Na^+ counterions at the last stage of the simulation (50 ns), displaying the three arms in different colours for visual clarity. The average gyration radius was 5.6 ± 0.3nm, t shows time in ns. (**E**) Representative MD snapshot of a single St-PGA-mUNO branch containing three equidistant mUNO peptides. Green spheres represent mUNO and a Licorice representation shows the linker. (**F**) mUNO rotation around the PGA chain for each of the three peptides (black, red, and green lines). (**G**) PGA chain secondary structure evolution, where red and brown regions show how mUNO perturbs the chain structure, turning alpha-helices into random coils.

Altogether, St-PGA-OG-mUNO and St-PGA-OG nanoconjugates possessed similar sizes by DLS, highly negative charges, and, according to simulations, displayed their three arms in an extended open structure. Our simulation analyses demonstrated that mUNO peptides induced a minimal effect on PGA structure and rotated around the PGA chain with considerable freedom. Overall, these findings suggest St-PGA-mUNO as a suitable platform for CD206 targeting.

179

180 **St-PGA-OG-mUNO targets CD206$^+$ TAMs and displays low Liver accumulation**

181 We next evaluated the potential of St-PGA-OG-mUNO to target CD206$^+$ TAMs in two
182 different TNBC models – an orthotopic TNBC model and an experimental metastasis of TNBC
183 model induced by intravenous (i.v.) injection of 4T1 cells. We administered St-PGA-OG-
184 mUNO or St-PGA-OG intraperitoneally (i.p.), allowed circulation for 6 h, and then analysed
185 tumour homing using confocal fluorescence microscopy. Our previous study provided the
186 rationale for the i.p. administration route, where we demonstrated that the i.p. administered
187 mUNO peptide exhibited a substantially longer half-life than intravenously (i.v.) administered
188 mUNO in the same mice (same strain, sex and age) used in this study[42].

189 In the orthotopic TNBC model, we observed a high colocalisation of OG/CD206 (Fig. 2A,
190 yellow signal) with St-PGA-OG-mUNO but a much lower colocalisation of OG/CD206 with
191 non-targeted St-PGA-OG (Fig. 2B) (0.57 and 0.21, respectively (Fig. 2M)). We observed a low
192 level of accumulation of St-PGA-OG-mUNO or St-PGA-OG in the liver (Fig. S3A, B). We
193 employed confocal image acquisition parameters throughout this study to visualise CD206 in
194 the tumour without signal saturation. Given the higher levels of CD206 in the tumour, imaging
195 with associated settings provides low CD206 visualisation in the liver. Using a higher image
196 intensity, we observed the expected CD206 signal in the liver (as expected from Kupfer cells
197 and sinusoid vessels) (Fig. S4A) and a saturated CD206 signal in the tumour (Fig. S4B).

198 Immunostaining for endogenous mouse IgG in the tumour and the liver indicated the leaky
199 nature of the tumour vasculature (Fig. S5A) compared to the liver vasculature (Fig. S5B) in the
200 4T1 model. A leaky tumour vasculature favours the hypothesis that St-PGA-OG-mUNO has a
201 more extended (both in time and space) access to CD206 in the tumour than in the liver. We
202 speculate that the leaky tumour vasculature combined with lower CD206 expression in the liver
203 than the tumour explains the low liver accumulation of St-PGA-OG-mUNO. St-PGA-OG-
204 mUNO did not accumulate in the lungs (Fig. S6A) or spleen (Fig. S6B); however, we did
205 observe some accumulation in the sentinel lymph node (SLN) (Fig. S6C) and the kidneys (Fig.
206 S6D). Of note, the observed kidney signal agrees with our prior studies that demonstrated the
207 renal excretion of St-PGA[47].

208 Importantly, we did not detect homing to M1 macrophages (CD86$^+$) or dendritic cells (CD11c$^+$,
209 DCs) with St-PGA-OG-mUNO (Fig. 2C, E) or with St-PGA-OG (Fig. 2D, F). In the
210 experimental metastasis of TNBC model, most of the cellular signal of St-PGA-OG-mUNO
211 associated with CD206$^+$ TAMs (Fig. 2G, yellow signal) when compared to St-PGA-OG (Fig.

212 2H) (OG/CD206 colocalisation 0.42 and 0.14, respectively, Fig. 2N). In this model, we also
213 observed no colocalisation between OG and CD86 (M1 macrophages) (Fig. 2I, J) or OG and
214 CD11c (DCs) (Fig. 2K, L) and the observed liver accumulation of St-PGA-OG-mUNO or St-
215 PGA-OG was low (Fig. S7).
216 One of the rationales behind the design of OximUNO was to increase mUNO targeting through
217 increased avidity and plasma half-life. To evaluate these aspects, we compared the homing of
218 St-PGA-OG-mUNO with a monomeric, carboxyfluorescein-labelled mUNO peptide (FAM-
219 mUNO). We note that even given the different nature of the fluorescent labels (OG on St-PGA-
220 OG-mUNO and fluorescein on FAM-mUNO), we did not use their native fluorescence as a
221 readout; instead, we used an antibody that recognises both FAM and OG; therefore, we do not
222 expect biases from potential differences in FAM and OG emissions.
223 We discovered that St-PGA-OG-mUNO (Fig. S8A) displayed significantly higher OG/CD206
224 colocalisation than for FAM/CD206 with FAM-mUNO (Fig. S8B) at 6 h (0.74 vs. 0.21,
225 respectively (Fig. 2O)). Additionally, we found that the OG/FAM mean signal per $CD206^+$ cell
226 was five times higher for St-PGA-OG-mUNO than FAM-mUNO (Fig. 2P). These findings
227 suggest that conjugating mUNO to the St-PGA backbone greatly improved receptor binding.
228 Plasma half-life analysis for i.p. administered St-PGA-OG-mUNO revealed a 4.5 h half-life
229 (Fig. 2Q), a value over two times longer than that observed after the i.p. administration of
230 FAM-mUNO in our previous study[42]. Overall, this finding suggests that conjugating onto St-
231 PGA increased the plasma half-life of mUNO peptide, a desirable feature that will improve in
232 vivo ligand targeting.

233

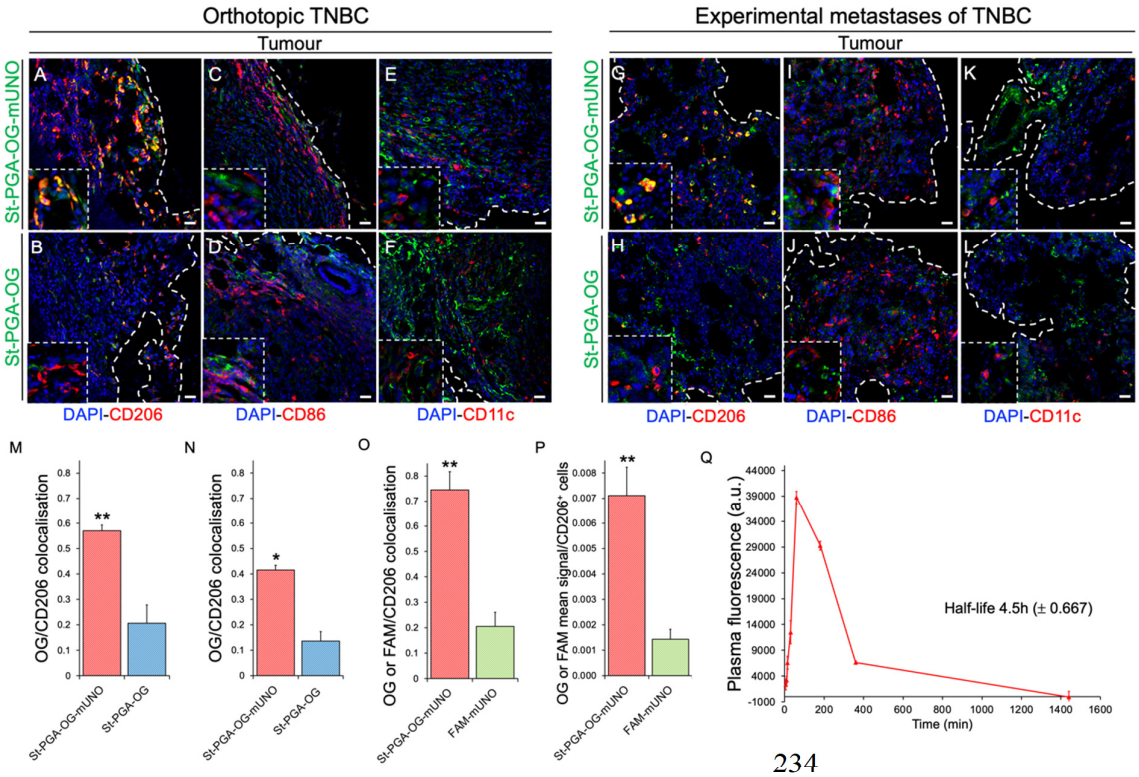

234

235 **Figure 2. St-PGA-OG-mUNO targets CD206⁺ TAMs in models of orthotopic TNBC and experimental**
236 **metastasis of TNBC and displays an extended plasma half-life.** Homing studies with i.p. administered St-PGA-
237 OG-mUNO (0.41 mg/0.5mL of PBS) or St-PGA-OG (0.35 mg/0.5mL of PBS), after 6 h of circulation. N=3 for
238 orthotopic TNBC and N=2 for experimental metastasis of TNBC. (**A-F**) Homing in orthotopic TNBC. (**A**) St-
239 PGA-OG-mUNO displayed high colocalisation between OG and CD206 (yellow signal), whereas (**B**) St-PGA-
240 OG displayed minimal colocalisation. St-PGA-OG-mUNO and St-PGA-OG did not show any homing to CD86⁺
241 cells (M1 macrophages) (**C, D**) nor CD11c⁺ cells (DCs) (**E, F**). (**G-L**) Homing study in the experimental metastasis
242 of TNBC. (**G**) St-PGA-OG-mUNO displayed high colocalisation with OG and CD206 (yellow signal), whereas
243 (**H**) St-PGA-OG showed minimal colocalisation. St-PGA-OG-mUNO and St-PGA-OG did not show any homing
244 to CD86⁺ cells (M1 macrophages) (**I, J**) or CD11c⁺ cells (DCs) (**K, L**). Scale bars represent 20 µm. (**M**) Graphs
245 depicting the quantification of CD206 and OG colocalisation in the orthotopic TNBC and (**N**) the experimental
246 metastasis of TNBC. (**O**) Quantification of colocalisation analysis for St-PGA-OG-mUNO or FAM-mUNO with
247 CD206 homing after 6 h of circulation, N=2 (30nmoles in OG and FAM, respectively). Colocalisation was
248 quantified using the Fiji programme and Pearson's coefficient (for more information see Materials and methods).
249 (**P**) Mean OG/FAM signal per CD206⁺ cell analysed using the ImageJ programme. (**Q**) Plasma fluorescence (in
250 the green channel) of i.p. administered St-PGA-OG-mUNO (dose 15nmoles in OG) in healthy Balb/c mice (N=3).
251 Error bars represent the standard error (SE) of the mean.
252

253 Administration of a higher dose of both nanoconjugates (0.82 mg/0.5mL St-PGA-OG-mUNO
254 and 0.7 mg/0.5mL St-PGA-OG) resulted in high CD206⁺ TAM targeting (Fig. S9A) albeit at

255 the expense of higher liver accumulation (Fig. S9C). For this reason, we employed lower
256 nanoconjugate doses (0.41 mg/0.5mL and 0.35 mg/0.5mL) for subsequent studies.
257 We next compared tumour homing of St-PGA-OG-mUNO to that of a therapeutic monoclonal
258 antibody by i.v. injecting anti-PDL1 in orthotopic 4T1 tumour-bearing mice and allowing
259 circulation for 24 h. We observed that administered anti-PDL1 accumulated in the tumour rim
260 (Fig. S10A, TR) but not in the tumour core (Fig. S10A, TC) even given expression of the
261 receptor (PDL1) in the tumour core (Fig. S10B, TC). The observed accumulation of St-PGA-
262 OG-mUNO in the tumour core (Fig. S10C) and receptor colocalisation (Fig. S10D), supported
263 the implementation of our platform as an efficient alternative to antibody-based therapies such
264 as anti-PDL1 or antibody-drug conjugates.
265 Overall, we demonstrated that St-PGA-OG-mUNO, homes to $CD206^+$ TAMs in both
266 orthotopic and experimental metastasis of TNBC models with no significant accumulation in
267 the liver. We also established that St-PGA-OG-mUNO does not target M1 macrophages or
268 DCs in the tumour, thereby providing evidence of high specificity for $CD206^+$ TAMs.
269
270
271 **OximUNO enhances the in vitro cytotoxicity of DOX on M2 macrophages**
272 St-PGA displays a large surface with multiple sites available for the conjugation of pro-
273 apoptotic or cytotoxic cargoes via bioresponsive polymer-drug linkers[48,49]. To selectively
274 deplete $CD206^+$ TAMs, we conjugated an apoptotic chemotherapeutic agent (DOX) to St-
275 PGA-mUNO to form St-PGA-DOX-mUNO (designated "OximUNO") (Fig. 3A, Scheme S2).
276 We conjugated DOX to St-PGA-mUNO using a hydrazone bond[48] to allow for site-specific
277 drug release in the acidic milieu of the endosomes/lysosomes[48,50].
278 To evaluate the effect of mUNO targeting, we included St-PGA-DOX as an untargeted control.
279 We employed ^{1}H NMR and UV-Vis analyses to evaluate the chemical identity of
280 nanoconjugates (Fig. S11A, B).
281 OximUNO displayed DOX and mUNO loadings of ~10% and ~4% in weight, respectively,
282 corresponding to around four DOX and seven mUNO molecules for every OximUNO.
283 OximUNO exhibited a size of ~40 nm and a highly negative surface charge of -40 mV (Fig.
284 3B, C). We obtained similar DOX loading, size by DLS, and surface charge values for St-PGA-
285 DOX (Fig. 3B, C).
286 The pH-sensitive hydrazone linker and the intrinsic biodegradability of St-PGA by lysosomal
287 protease cathepsin B are expected to secure DOX release from OximUNO after cell

288 internalisation[51]. Hence, we studied DOX release kinetics from OximUNO in the presence of
289 acidic pH (pH 5) and cathepsin B using liquid chromatography-mass spectrometry (LC-MS,
290 Fig. S12A-G). As we aimed for the i.p. administration of OximUNO, we assessed DOX release
291 in intraperitoneal fluid (i.p. fluid) (Fig. 3D). At pH 5, we observed a sustained DOX release in
292 the first 8 h (reaching a plateau at 15%), thereby demonstrating the suitability for endo-
293 lysosomal drug delivery. DOX release in the presence of cathepsin B displayed comparable
294 values in the first 8 h (~13%), followed by a plateau and a reduced rate in the following hours
295 (~13% cumulative release at 72 h). Importantly, OximUNO exhibited negligible drug release
296 in both physiological conditions evaluated (PBS and i.p. fluid) (Fig. 3D).
297 We next evaluated the in vitro cytotoxicity of OximUNO and St-PGA-DOX in primary human
298 blood monocyte-derived M2 and M1 macrophages. To emulate the in vivo concentration that
299 provided optimal $CD206^+$ TAM targeting with minimal liver accumulation (30 µM in OG), we
300 evaluated conjugates at 33 µM DOX loading. Our previous studies comparing other mUNO-
301 targeted vs. untargeted polymeric nanosystems[44] demonstrated that the highest targeted uptake
302 in primary M2 macrophages occurred after an interval of 10 to 30 min. For this reason, we used
303 an incubation time of 15 min for these experiments.
304 Under these conditions, free DOX did not display toxicity to M2 or M1 macrophages (Fig. 3E,
305 purple bar); in contrast, OximUNO displayed significantly higher toxicity against M2
306 macrophages than DOX (52%) and St-PGA-DOX (33%) (Fig. 3E, red bar) while OximUNO
307 induced two times less toxicity than St-PGA-DOX in M1 macrophages. Interestingly, St-PGA-
308 DOX showed higher toxicity in M1 than M2 macrophages (Fig. 3E, blue bar), possibly because
309 M1 macrophages display greater phagocytic activity than M2 macrophages[52,53], which might
310 also explain the 60% cell viability following OximUNO treatment of M1 macrophages (Fig.
311 3E, red bar). We observed a similar trend using a higher concentration of DOX (100µM);
312 however, free DOX displayed significant toxicity in M2 macrophages at this higher
313 concentration (Fig. 3E, purple bar). These results provide evidence that OximUNO displayed
314 increased toxicity towards M2 macrophages when compared to St-PGA-DOX or DOX alone.
315 We note that OximUNO induced a degree of in vitro toxicity towards M1 macrophages;
316 however, our homing studies revealed that St-PGA-OG-mUNO did not target M1 macrophages
317 in vivo (Fig. 2C, I).
318 CD206 is also expressed on other macrophage populations in other organs, although at lower
319 levels than for M2 TAMs. We performed in vitro cytotoxicity studies of OximUNO on non-
320 polarised blood monocyte-derived macrophages, designated "M0", which we previously
321 showed express CD206, at levels lower than in M2[42]. These assays revealed moderate toxicity

322 of OximUNO to M0 macrophages (Fig. S13); however, the fact that St-PGA-OG-mUNO did
323 not target the lung, liver, or spleen (section 2) suggests that OximUNO will not affect the
324 macrophage populations of those organs.
325 We also evaluated the hepatic and renal safety profile of a single administration of OximUNO
326 (at doses corresponding to 2 mg/kg and 4 mg/kg DOX) by analysing creatinine (Crea) and
327 alanine aminotransferase (ALAT) levels 48 h after i.p. administration in healthy mice (Fig. 3F).
328 These doses did not induce toxic levels of Crea or ALAT compared to the values reported in
329 the literature[54] or the reference values for the female Balb/c reported in the Mouse Phenome
330 Database by The Jackson Laboratory[55] or Charles River facilities[56]. However, increased ALAT
331 levels with the higher dose, prompted the selection of the OximUNO dose corresponding to 2
332 mg/kg DOX for further in vivo studies.
333
334

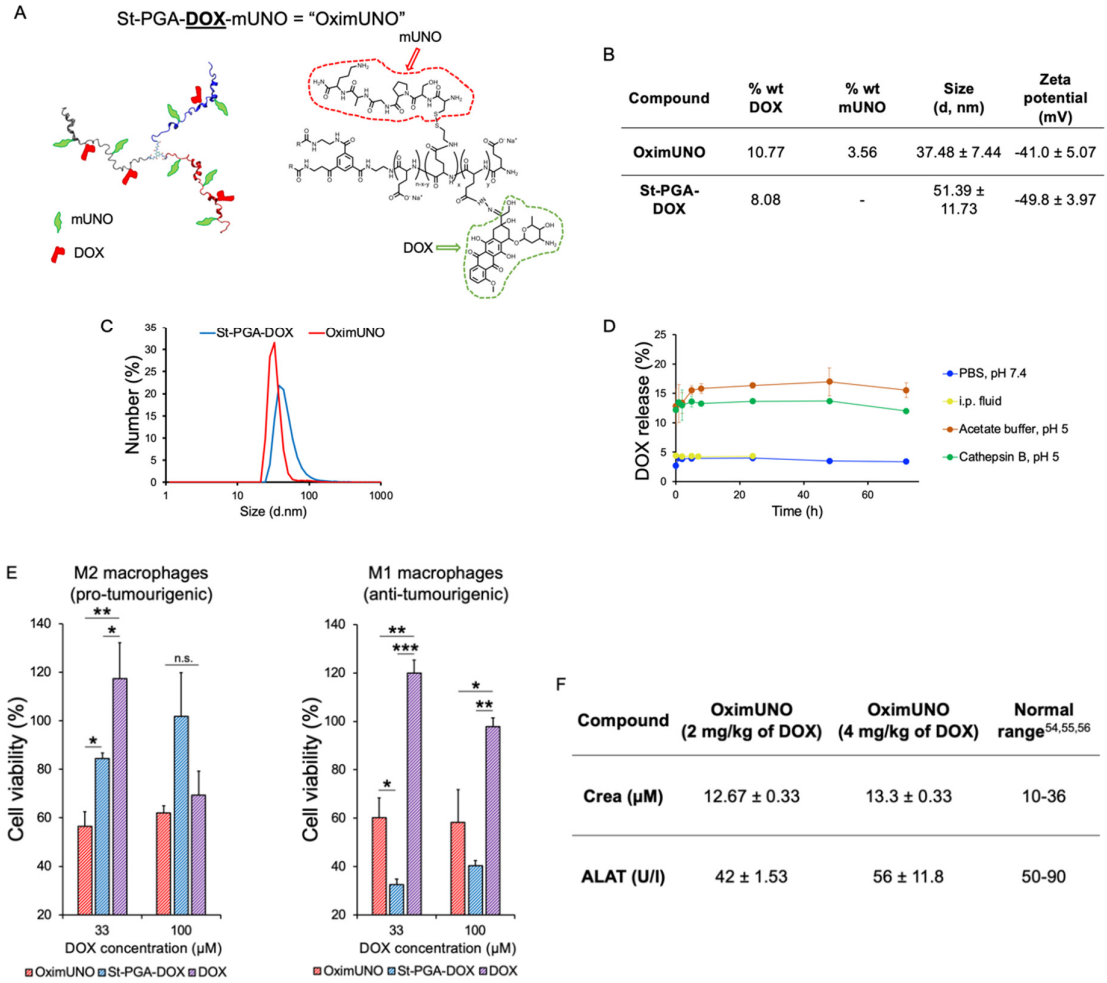

Compound	% wt DOX	% wt mUNO	Size (d, nm)	Zeta potential (mV)
OximUNO	10.77	3.56	37.48 ± 7.44	-41.0 ± 5.07
St-PGA-DOX	8.08	-	51.39 ± 11.73	-49.8 ± 3.97

Compound	OximUNO (2 mg/kg of DOX)	OximUNO (4 mg/kg of DOX)	Normal range[54,55,56]
Crea (μM)	12.67 ± 0.33	13.3 ± 0.33	10-36
ALAT (U/l)	42 ± 1.53	56 ± 11.8	50-90

335 **Figure 3. OximUNO enhances the in vitro efficacy of DOX on M2 macrophages.** (**A**) Simplified form of
336 OximUNO (left) and molecular structure (right) showing St-PGA decorated with mUNO (red) and DOX (green).

337 (**B**) Table showing DOX loading, mUNO loading, size (as measured by DLS), and charge (as measured by Zeta
338 potential) of both nanoconjugates in PBS. (**C**) A DLS graph for measurements shown in (B), indicating the
339 uniform size of OximUNO and St-PGA-DOX. (**D**) DOX release from OximUNO showing the drug release in
340 PBS, i.p. fluid, acetate buffer or in the presence of cathepsin B. (**E**) In vitro cytotoxicity in primary human M2
341 (left panel) or M1 (right panel) macrophages after treatment with OximUNO (red bars), St-PGA-DOX (blue bars),
342 and DOX (purple bars) following a 15 min incubation, washed, cultured for additional 48 h, and then analysed
343 for cell viability as evaluated by MTT assay. (**F**) Hepatic and renal toxicology serum levels of Crea and ALAT
344 48 h after i.p.-administration of OximUNO (at two different doses in DOX: 2 mg/kg and 4 mg/kg) in healthy
345 Balb/c mice (N=3). Error bars represent the SE of the mean.
346
347 In summary, the conjugation of mUNO and DOX to the St-PGA backbone to yield OximUNO,
348 enhanced the in vitro efficacy of DOX towards M2 macrophages with no in vivo renal or
349 hepatic toxicity observed.
350
351
352 **OximUNO treatment of orthotopic TNBC depletes CD206$^+$ TAMs, inhibits**
353 **tumour progression and attenuates immunosuppression**
354 The findings of the in vivo homing and in vitro cytotoxicity studies supported the subsequent
355 evaluation of OximUNO in the orthotopic TNBC model. When tumours reached 25 mm^3, we
356 treated mice with i.p. injections of OximUNO, St-PGA-DOX, or DOX, at 2 mg/kg DOX every
357 other day for eighteen days. Encouragingly, OximUNO treatment significantly reduced
358 primary tumour volume growth kinetics (Fig. 4A, red line) compared to DOX, St-PGA-DOX,
359 and PBS. Furthermore, only the OximUNO treatment significantly reduced final tumour
360 weight (Fig. 4B) compared to the untreated group. We assigned this encouraging therapeutic
361 effect to mUNO-mediated targeting, as animals treated with the untargeted St-PGA-DOX
362 possessed tumour volumes (Fig. 4A, blue line) similar to the PBS group (Fig. 4A, black line).
363 Furthermore, OximUNO treatment did not affect mouse bodyweight, whereas treatment with
364 DOX induced a significant decrease in mouse bodyweight starting from day twenty-one post-
365 inoculation (p.i.) until the end of the treatment (Fig. 4C).
366 Histological analysis of lungs from treated mice (Fig. S14 shows an H&E stain from a healthy
367 lung for comparison) revealed that OximUNO also influenced the extent of pulmonary
368 metastases (Fig. 4D), as it elicited the highest reduction in the metastatic lung area and nodule
369 number ($p=0.06$ vs. PBS and $p=0.06$ vs. DOX, respectively (Fig. 4E, F)). Meanwhile,
370 immunofluorescence (IF) microscopy revealed no significant changes in CD31 expression in
371 tumours (Fig. S15A, B), but significantly fewer CD31$^+$ structures in the OximUNO-treated

372 mice compared to DOX-treated mice (Fig. S15A, C), suggesting that the reduction in nodule
373 number in the OximUNO group (of Fig. 4F) may be mediated by the lower vascularisation in
374 the primary tumour. Importantly, histological analysis revealed no cardiotoxicity in any
375 treatment groups (Fig. S16). IF analysis revealed that only OximUNO significantly reduced
376 the CD206 expression (assigned to $CD206^+$ TAMs), compared to PBS (Fig. 4G, J).
377 Interestingly, treatment with DOX upregulated CD206 expression (Fig. 4G, J), which agrees
378 with previous reports that demonstrated an increase in the number of $CD206^+$ TAMs following
379 chemotherapy[24].
380 Notably, only OximUNO treatment significantly increased CD8 expression (a marker of
381 cytotoxic T cells (CTLs)) compared to PBS and DOX treatment (Fig. 4H, K). Unexpectedly,
382 St-PGA-DOX treatment increased the expression of FOXP3, a marker for regulatory T cells
383 (Tregs) (Fig. 4I, L). Analysis of the CD8/FOXP3 expression ratio revealed that OximUNO
384 treatment resulted in a five-fold increase compared to St-PGA-DOX or DOX treatment (Fig.
385 4M), suggesting that OximUNO stimulated a shift in the immune landscape towards
386 immunostimulation. Of note, in all cases, we normalised the quantification of marker
387 expression using immunofluorescent images to the tissue area to account for different amounts
388 of tissue in different images.
389
390

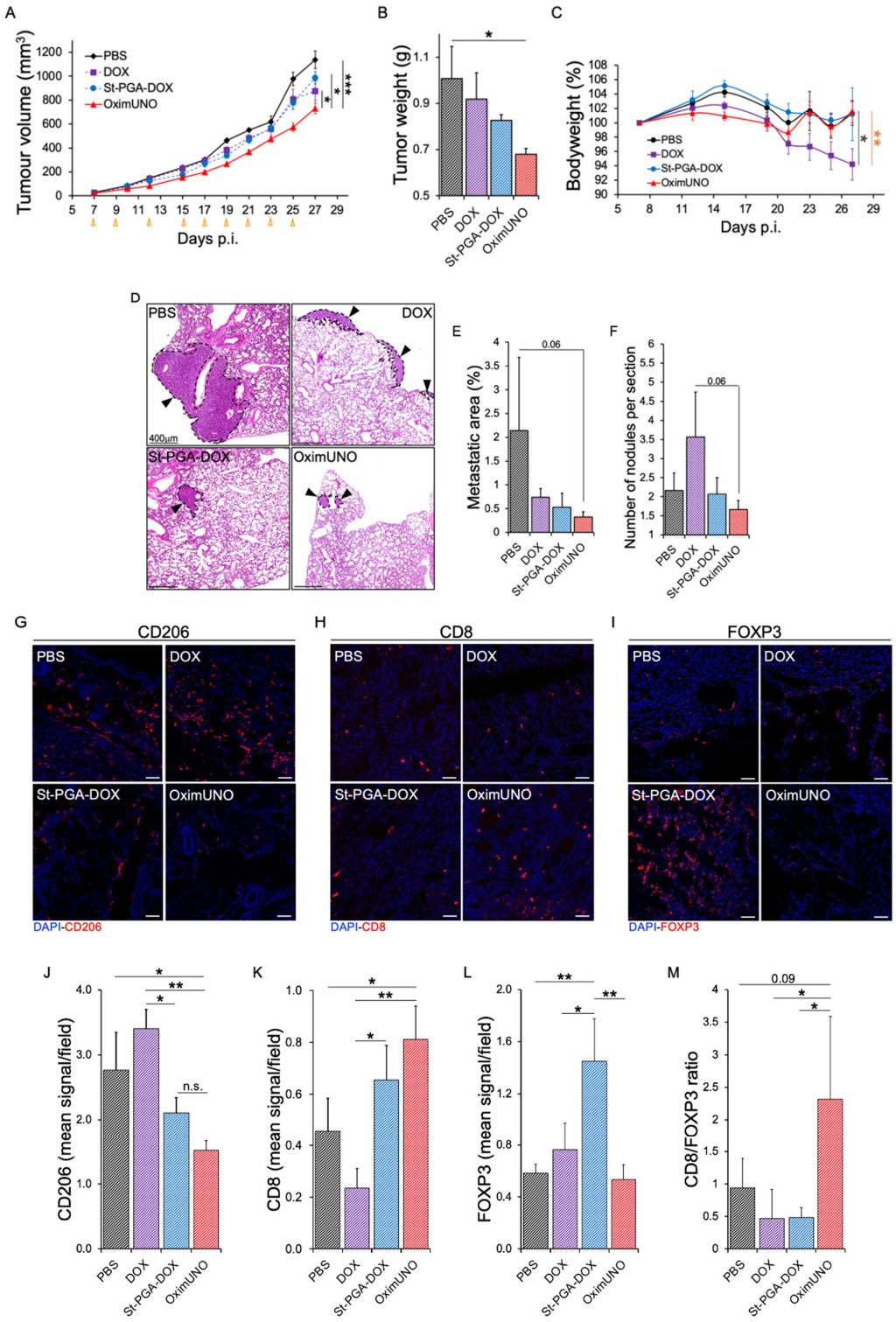

Figure 4. OximUNO treatment reduces primary tumour growth and pulmonary metastases and alleviates immunosuppression. Treatment with OximUNO, St-PGA-DOX, or DOX at 2 mg/kg DOX in mice bearing orthotopic TNBC tumours (N=5). I.p. injections began when tumours reached 25 mm^3 and were performed every other day to give a total of nine injections. (**A**) Primary tumour volume progression during treatment. Orange

396 arrows indicate injection days. (**B**) Primary tumour weight at the experimental endpoint, demonstrating a
397 significantly smaller weight for OximUNO-treated mice (red bar) than other groups. (**C**) Mouse bodyweight
398 analysis suggests the safety of OximUNO treatment (red line); meanwhile, DOX-treatment induced a significant
399 reduction in bodyweight by the experimental endpoint (purple line). Dark grey ∗ DOX vs. PBS, orange ∗ DOX
400 vs. St-PGA-DOX. (**D**) Representative H&E images showing pulmonary metastases for all groups (scale bars =
401 400 μm); OximUNO treatment associated with the smallest metastatic area (**E**) and the lowest number of average
402 nodules per lung (**F**). (**G-I**) Representative confocal microscopy images demonstrating the expression of (**G**)
403 CD206, (**H**) CD8, and (**I**) FOXP3. Scale bars = 50 μm. (**J-M**) Quantification of confocal microscopy images for
404 the expression of (**J**) CD206, (**K**) CD8, and (**L**) FOXP3. (**M**) Graph of CD8/FOXP3 expression ratio showing a
405 shift in the immune profile. Quantification was performed using the ImageJ programme from at least three images
406 per mouse and five mice per group. Error bars represent the SE of the mean.
407
408 By targeting CD206$^+$ TAMs with DOX via OximUNO treatment, we increased the efficacy
409 and reduced the toxicity of DOX in the orthotopic TNBC model. Our results also suggest that
410 the depletion of CD206$^+$ TAMs by OximUNO elicited an immunostimulatory shift.
411
412
413 **OximUNO treatment of experimental TNBC metastasis reduces CD206$^+$ TAMs**
414 **number, tumour burden and attenuates immunosuppression**
415 We next evaluated the effect of OximUNO on experimental TNBC metastasis using GFP-
416 labelled 4T1 cells. We treated mice every other day with i.p. injections of OximUNO, St-PGA-
417 DOX, or DOX, starting from day four p.i. and sacrificed mice on day eighteen p.i. Analysis of
418 whole lung fluorescence in the green channel revealed that OximUNO treatment induced the
419 lowest GFP fluorescence, indicating a lower level of pulmonary metastases (Fig. 5A).
420 Representative macroscopic images also provided evidence for a reduction in metastases (Fig.
421 5B). Confocal fluorescence microscopy of lungs confirmed the trend observed with whole lung
422 fluorescence, showing fewer GFP fluorescent nodules in the OximUNO-treated group (Fig.
423 5C). Furthermore, histological analysis of lungs displayed the lowest number of pulmonary
424 nodules for OximUNO-treated mice (Fig. 5D). Mice treated with the untargeted St-PGA-DOX
425 and free DOX showed a significant decrease in bodyweight, resulting in a 19% (Fig. 5E, blue
426 line) and 17% loss (Fig. 5E, purple line), respectively; meanwhile, OximUNO-treated mice
427 displayed lower bodyweight loss (Fig. 5E, red line).
428 We next employed flow cytometry (FC) to analyse the effect of different treatments on the
429 immune cell populations in whole lungs. This analysis demonstrated that OximUNO treatment
430 significantly lowered the percentage of M2 TAMs (CD206$^+$) (Fig. 5F) but did not significantly

431 impact the percentage of M1 TAMs, CTLs, or Tregs (Fig. 5G-I). We observed the same trend
432 when we expressed these populations as total cell counts (Fig. S17-S20).
433 To evaluate if OximUNO affected $CD206^+$ macrophages other than M2 TAMs, we analysed
434 the state of splenic macrophages from this treatment study using FC. This analysis revealed no
435 significant differences in the CD206/CD86 populations between the OximUNO-treated mice
436 and PBS-treated mice (Fig. S21A-C).
437 While FC analysis informs on the immune status of the whole lung, it does not provide specific
438 information regarding the TME. To characterise the immune landscape of the TME, we next
439 analysed the expression of markers for TAMs, CTLs, and Tregs in pulmonary nodules using
440 IF. This analysis revealed significantly lower CD206 expression in OximUNO-treated mice
441 than PBS-treated mice (Fig. 5J, N), providing evidence for a robust reduction in the number of
442 $CD206^+$ TAMs in the TME. Importantly, and similarly to OximUNO treatment in the
443 orthotopic TNBC mouse model, OximUNO elicited the highest expression of CD8 (Fig. 5K,
444 O). OximUNO and St-PGA-DOX treated mice demonstrated significantly lower lung FOXP3
445 expression than PBS- and DOX-treated mice (Fig. 5L, P). OximUNO-treated mice displayed
446 between a two- and three-times higher CD8/FOXP3 expression ratio than St-PGA-DOX and
447 DOX, and nearly seven-times higher than PBS (Fig. 5M). Therefore, our IF analysis in the
448 pulmonary tumour nodules suggested that OximUNO triggered a shift in the immune profile
449 of the TME towards immunostimulation.
450
451
452
453
454
455
456
457
458
459
460

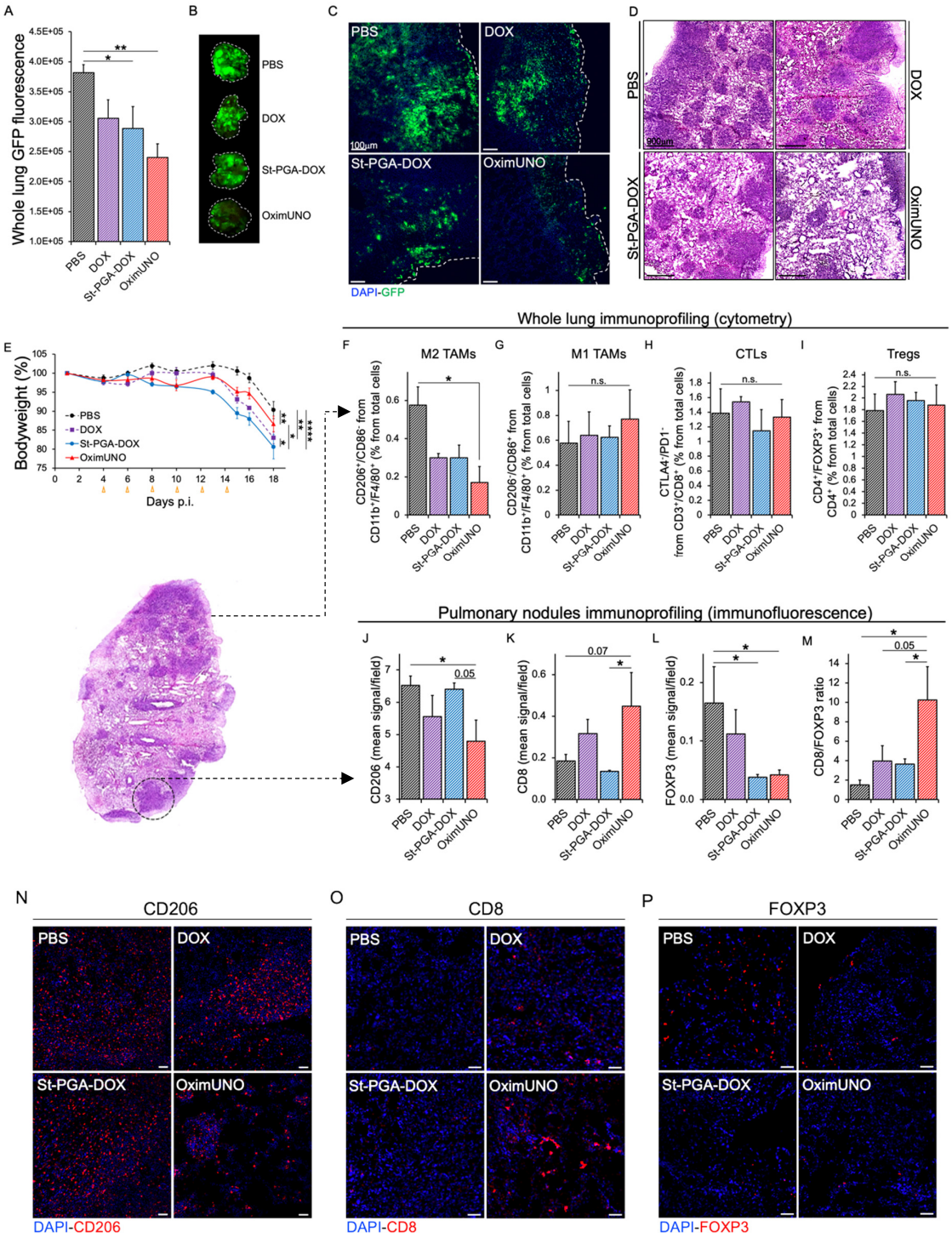

Figure 5. OximUNO treatment in experimental metastasis of TNBC significantly reduces CD206⁺ TAM number and tumour burden and alleviates immunosuppression. Treatment with OximUNO, St-PGA-DOX, or DOX at 2 mg/kg DOX in the experimental metastasis of TNBC model, created using GFP-labelled 4T1 cells (N=6). I.p. injections began on day four p.i. and were performed every other day to give a total of six injections. (**A**) Quantification of whole lung GFP fluorescence at the experimental endpoint using the ImageJ programme

468 (N=6). (**B**) Representative macroscopic photographs of GFP fluorescence in the lungs. (**C**) Representative
469 confocal microscopy images of GFP expression, scale bars = 100 μm. (**D**) Representative H&E images showing
470 pulmonary metastases for all groups (scale bars = 900 μm). (**E**) Mouse bodyweight analysis, demonstrating
471 significantly lower bodyweight lost with OximUNO (red line) compared with St-PGA-DOX-treated mice (blue
472 line) and DOX-treated mice (purple dotted line). Orange arrows indicate injection days. (**F-I**) FC analysis on three
473 right lungs per group. (**F**) M2 TAMs ($CD206^+$), (**G**) M1 TAMs, (**H**) CTLs and (**I**) Tregs. (**J-M**) IF analysis on the
474 pulmonary tumour nodules to detect the expression of (**J**) CD206, (**K**) CD8, and (**L**) FOXP3. (**M**) Graph showing
475 CD8/FOXP3 expression ratio. IF images quantified using the ImageJ programme from at least five images per
476 mouse and three mice per group. (**N-P**) Representative confocal microscopy images for (**N**) CD206, (**O**) CD8,
477 and (**P**) FOXP3. Scale bars = 50 μm. Error bars represent the SE of the mean.
478
479 By targeting DOX to $CD206^+$ TAMs in experimental TNBC metastases, we increased the
480 efficacy and reduced the toxicity of DOX, as OximUNO treatment associated with the presence
481 of fewer pulmonary tumour lesions and less bodyweight loss when compared to treatment with
482 untargeted St-PGA-DOX and DOX. Our results suggest that the observed therapeutic effect
483 derived from $CD206^+$ TAM depletion, which elicited an immunological shift in the TME.
484
485
486 **DISCUSSION**

487 To date, TNBC remains an aggressive breast cancer subtype[3] with few treatment options, with
488 conventional chemotherapy representing the current standard of care[20]. ICIs for TNBC have
489 provided only modest improvements in complete response and progression-free survival in a
490 small subset of TNBC patients[9,12,15,16]. Targeting TAMs can potentiate ICIs and other
491 modalities and, therefore, represents an intense area of study[57–61]; however, TAMs represent a
492 diverse population[62–64], and which TAM subtype to target remains under investigation.
493 Promising TAM-focused interventions under clinical evaluation include antibody-mediated
494 depletion of TREM2-expressing TAMs (clinical trial identifier: NCT04691375). Antibody
495 blockade of Clever-1 on M2 TAMs stimulated an M2→M1 switch in TNBC models (4T1) and
496 synergised with the PD-1 blockade[67]. Appealing studies have used anti-CD163 antibodies to
497 target TAMs[65] by decorating DOX-carrying liposomes with anti-CD163, to deplete TAMs and
498 potentiate ICIs in melanoma. Given our data comparing the tumour penetration of an anti-
499 PDL1 antibody vs. St-PGA-OG-mUNO, anti-CD163 systems may also display lower tumour
500 accumulation than St-PGA-OG-mUNO and OximUNO. Strategies targeting generic TAM
501 markers such as CSF1R and CCR2 have shown side effects and limited efficacy.

502 Motivated by the preponderance of the mannose receptor in tumourigenic/metastatic TAMs in
503 breast cancer[68–70], here, we set out to deplete CD206$^+$ TAMs in aggressive and metastatic
504 TNBC models and study the consequences on the progression and immunosuppressive state of
505 the tumour. To target CD206, a CD206-binding nanobody was developed by Ginderachter et
506 al.[71] which showed homing to CD206$^+$ TAMs in in vivo models of lung and breast cancers[71].
507 Navidea Inc. engineered a mannosylated compound[72] (Manocept™), that forms part of the
508 FDA-approved contrast agent Lymphoseek®. Unfortunately, mannose-based ligands have
509 other binding partners besides CD206, including CD209 in intestinal and genital tissues[45], and
510 can target dendritic cells[46]. Riptide Inc. also designed a peptide (RP-182) that binds to CD206;
511 however, the peptide also binds to RelB, Sirp-α and CD47[73].
512 We recently identified and described a short peptide called mUNO (sequence: CSPGAK) that
513 targets mouse[41] and human CD206[43] at a different binding site than for mannose on CD206[43].
514 We identified mUNO from an in vivo screen using a peptide library in mice bearing metastatic
515 breast cancer; we subsequently described how mUNO homed to CD206$^+$ TAMs in other solid
516 tumour models[41,74] and in early-stage models of TNBC[42] displaying low liver accumulation.
517 We envisioned that conjugating mUNO to St-PGA would significantly enhance targeting
518 through the avidity effect and increased plasma half-life[75].
519 Compared to synthetic polymers such as N-(2-hydroxypropyl) methacrylamide, polypeptide-
520 based nanocarriers show several benefits, including biodegradability, lower immunogenicity,
521 and a lack of long term-accumulation, and the number of polypeptide-based constructs reaching
522 clinical evaluation has significantly increased in recent years[76–78]. We employed St-PGA-based
523 nanoconjugates with three linear chains (~50 glutamic acids each) linked to a central core.
524 Overall, the safety, lack of toxicity, and biodegradability of St-PGA meet FDA approval
525 criteria[79]. A previous screen of PGA structures suggested that larger architectures enhanced
526 plasma half-life and increased bioavailability through a higher hydrodynamic volume that
527 reduces rapid renal clearance[47,80]. Of note, an extended plasma half-life will be advantageous
528 when targeting the continuously replenished TAM cell type[81,82].
529 St-PGA-OG-mUNO, a fluorescent counterpart of OximUNO, can be easily monitored by
530 immunostaining for OG or detecting native OG fluorescence (as for the half-life study). Given
531 weak DOX fluorescence and the inability to detect DOX with an antibody, we first designed
532 St-PGA-OG-mUNO for validation purposes. We then exchanged OG for DOX to generate St-
533 PGA-DOX-mUNO, referred to as "OximUNO".
534 Our studies demonstrated that St-PGA-OG-mUNO displayed a far greater plasma half-life and
535 specificity to CD206$^+$ TAMs than free mUNO and avoided CD86$^+$ M1 TAMs and CD11c$^+$

536 DCs, an important fact since M1 TAMs display anti-tumourigenic activity[25], and CD11c$^+$ DCs
537 participate in antigen presentation[83]. In line with these observations, the computational analysis
538 indicated that mUNO peptides are available to a receptor and sweep a vast space (130°) around
539 PGA. Altogether this data demonstrates the benefit of conjugating mUNO to St-PGA. While
540 previous studies have reported the St-PGA nanocarrier[47,79] and the mUNO targeting peptide[42],
541 this work represents the first design of a peptide-targeted St-PGA nanosystem. Regarding the
542 administration route of peptide-guided St-PGA nanosystems, in the future we also wish to
543 evaluate the i.v. route, which, barring the case of intraperitoneal chemotherapy, represents a
544 more clinically translatable route to deliver cancer therapies.
545 In the OximUNO system, drug release studies revealed only 15% DOX release, which agrees
546 with our previous studies[48,50] but suggests room for improvement, which may come from using
547 longer polymer-drug linkers such as EMCH (N-ε-maleimidocaproic acid hydrazide) moiety[48,50]
548 or from the use of external triggers[84–86]. Unexpectedly, we failed to observe a significant
549 increase in DOX release in the presence of cathepsin B with respect to the hydrolytic
550 conditions; we hypothesise that the nanoconjugate conformation slows down proteolytic
551 degradation, hampering in vitro quantification within the studied timeframe[47].
552 Our in vivo efficacy studies showed that, strikingly, the sole depletion of CD206$^+$ TAMs with
553 OximUNO alleviated tumoural immunosuppression and reduced dissemination and growth,
554 confirming the pro-tumoural and immunosuppressive roles assigned to CD206$^+$ TAMs in the
555 literature and reaffirming the importance of targeting this particular TAM subset. Additionally,
556 the observed reduction in the number of CD206$^+$ TAMs and CD31$^+$ structures for OximUNO
557 agrees with the established angiogenic role of CD206$^+$ TAMs[24].
558 From a safety point of view, we found that the OximUNO nano-formulation of DOX had the
559 least negative impact on mouse bodyweight compared to free DOX or the untargeted nano-
560 formulation St-PGA-DOX. Additionally, OximUNO did not alter Crea or ALAT levels,
561 indicating the absence of acute hepatic or renal toxicity. Our data suggest that the signal
562 observed in the kidneys for St-PGA-OG-mUNO (consistent with the previously reported
563 excretion of St-PGA[47,79]) did not translate into acute renal toxicity for OximUNO. These are
564 relevant findings as DOX induces cell death and tissue damage not only in the heart but also in
565 the liver and kidneys[87]. OximUNO displayed moderate toxicity to un-polarised macrophages
566 in vitro; however, OximUNO did not affect or alter the macrophage populations of the spleen
567 in vivo, in agreement with the absence of spleen targeting we observed for St-PGA-OG-
568 mUNO.

569 Most preclinical studies evaluating the effect of M2 TAM targeted monotherapy in the 4T1
570 mouse model have either not shown efficacy on secondary tumours[88,89], a lack of efficacy in
571 primary tumours or metastases in the case of anti-CLEVER-1[67], or a pro-metastatic effect in
572 the case of anti-CSF1R[90]. Hence, along with anti-MARCO therapy[91], OximUNO constitutes
573 one of the few reports of an M2 TAM targeted monotherapy affecting both primary and
574 secondary tumours in the 4T1 mouse model.
575 Beyond TAM depletion, we show that St-PGA-mUNO represents an attractive platform to
576 carry additional therapeutic payloads other than DOX, which could include M2→M1
577 polarising agents such as TLR7 agonists[44,92], beta-emitting radiotherapeutic agents such as
578 dodecanetetraacetic acid-chelated ^{177}Lu [93], or photosensitisers used in photodynamic therapy[84–
579 86]. We also envisage the combination of TAM-depletion via OximUNO administration together
580 with current chemotherapy regimens to prevent dissemination and relapse.
581 Taking OximUNO as a proof-of-concept, our data support the peptide-targeted St-PGA design
582 reported here as a new targeted nanosystem that could target other receptors by exchanging the
583 targeting peptide.
584
585
586 # MATERIALS AND METHODS
587 **Reagents and solutions**
588 The peptides mUNO (sequence: CSPGAK-COOH) and FAM-mUNO (FAM-Ahx-CSPGAK-
589 COOH) were purchased from TAG Copenhagen and doxorubicin (DOX) from Sigma-Aldrich.
590 St-PGA was kindly provided by Polypeptide Therapeutic Solution S.L. (PTS, Valencia, Spain).
591 See the Supplementary Information for information on all other reagents and solutions.
592 Mayer's haematoxylin solution was prepared by dissolving 5 g of aluminium potassium
593 sulphate dodecahydrate (Merck Millipore, cat. 1010421000) in 100 mL of water, and adding 1
594 g of haematoxylin (Merck, cat. H9627). After complete dissolution, 0.02 g of sodium iodide
595 (Merck, cat. 1065230100) was added and completely dissolved. Then, 2 mL of acetic acid
596 (Sigma-Aldrich, cat. 33209) was added, and then the solution was boiled and then cooled. Once
597 ready to use, the solution was filtered using a 0.45 μm filter.
598 Eosin (5%) solution was prepared by dissolving 0.5 g of Eosin Y (Sigma-Aldrich, cat. 230251)
599 in 99 mL water/1 mL acetic acid.
600
601 **Cell culture and experimental animals**

602 4T1 cells were purchased from ATCC, and 4T1-GFP cells were a gift from Ruoslahti
603 laboratory (Sanford-Burnham-Prebys Medical Discovery Institute, La Jolla, USA). 4T1 and
604 4T1-GFP cells were cultured in RPMI-1640 medium (Gibco by Life Technologies, cat. 72400-
605 021) supplemented with 10% v/v foetal bovine serum (FBS, Capricorn Scientific, cat. FBS-
606 11A) and 100 IU/mL penicillin/streptomycin (Capricorn Scientific, cat. PS-B) at 37 °C in the
607 presence of 5% CO_2. For all animal experiments, 8-12-week-old female Balb/c mice were used.
608 Animal experiment protocols were approved by the Estonian Ministry of Agriculture (Project
609 #159). All methods were performed in accordance with existing guidelines and regulations.
610
611 **Tumour models**
612 Two tumour models were used for homing studies: the orthotopic TNBC model, where $1x10^6$
613 4T1 cells in 50 µL of phosphate-buffered saline (PBS, Lonza, cat. 17-512F) were
614 subcutaneously (s.c.) injected into the fourth mammary fat pad, and the experimental metastasis
615 of TNBC model, where $5x10^5$ 4T1 cells in 100 µL of PBS were injected i.v. into Balb/c mice.
616 Two tumour models were used for treatment studies: the orthotopic TNBC model where $5x10^4$
617 4T1 cells in 50 µL of PBS were injected s.c. into fourth mammary fat pad; and the experimental
618 metastasis of TNBC model where $2x10^5$ 4T1-GFP cells in 100 µL of PBS were i.v. injected.
619
620 **Nanoconjugate synthesis and characterisation**
621 In vivo homing studies used St-PGA-OG and St-PGA-OG-mUNO, while in vitro cytotoxicity
622 and in vivo treatment studies used St-PGA-DOX and St-PGA-DOX-mUNO ("OximUNO").
623 DOX denotes doxorubicin. Detailed synthetic procedures for single nanoconjugates can be
624 found in Supplementary Information.
625
626 **Physico-chemical characterisation methods**
627 Nuclear magnetic resonance (NMR) spectroscopy: NMR spectra were recorded at 27 °C (300
628 K) on a 300 UltrashieldTM from Bruker. Data were processed with Mestrenova software.
629 Sample solutions were prepared at the desired concentration in D_2O or D_2O supplemented with
630 $NaHCO_3$ (0.5 M).
631 UV-Visible (UV-Vis) analysis: UV-Vis measurements were performed using JASCO V-630
632 spectrophotometer at 25 °C with 1 cm quartz cells and a spectral bandwidth of 0.5 nm. Spectra
633 analysis was recorded three times in the range of 200–700 nm.

634 Fluorescence analysis: Fluorescence analysis was performed using a JASCO FP-6500
635 spectrofluorimeter at 25 ºC with 1 cm quartz cells.
636 Dynamic Light Scattering (DLS): Size measurements were performed using a Malvern
637 ZetasizerNano ZS instrument, supported by a 532 nm laser at a fixed scattering angle of 173°.
638 Nanoconjugate solutions (0.1 mg/mL) were freshly prepared in PBS (10 mM phosphate, 150
639 mM NaCl), filtered through a 0.45 µm cellulose membrane filter, and measured. Size
640 distribution was measured (diameter, nm) for each polymer in triplicate. Automatic
641 optimisation of beam focusing and attenuation was applied for each sample.
642 Zeta potential measurements: Zeta potential measurements were performed at 25 °C using a
643 Malvern ZetasizerNano ZS instrument, equipped with a 532 nm laser using disposable folded
644 capillary cells, provided by Malvern Instruments Ltd. Nanoconjugate solutions (0.1 mg/mL)
645 were freshly prepared in 1 mM KCl. Solutions were filtered through a 0.45 µm cellulose
646 membrane filter. Zeta potential was measured for each sample per triplicate.
647
648 **Molecular dynamics simulations**
649 Molecular dynamics (MD) simulations of PGA chains, and mUNO peptide were carried out
650 using the ff19SB force field[95] in the Amber20 MD engine[96]. The nanoconjugate system was
651 neutralised using Na+ ions and hydrated to account for a total of ~920,000 atoms (~300,000
652 TIP3P water molecules) in a truncated octahedral box. A hydrogen mass repartitioning strategy
653 was applied on the resulting topology, allowing us a 4 fs integration time step[97]. Standard
654 minimisation and equilibration protocols were used to reach 300 K and 1 atm., followed by 50
655 ns of production MD run. The simulations were run under the NVT ensemble (constant number
656 of particles, volume, and temperature through Berendsen thermostat[98]), considering periodic
657 boundary conditions. The SHAKE algorithm was used to fix hydrogen atoms[99]. The non-bound
658 cut-off value was set to Angstrom. The central moiety was parametrised using the
659 recommended protocol for the Amber force field. It was necessary to introduce amide bond,
660 angle and dihedral terms using the ParmEd module to establish the bond of the central molecule
661 to the PGA chains.
662
663 **Tumour homing studies**
664 Tumours were induced as described in the tumour model section. Tumour homing studies were
665 performed on mice bearing orthotopic TNBC or experimental metastasis of TNBC. Ten days
666 p.i. of the orthotopic TNBC or the experimental metastasis of TNBC model, mice were i.p.
667 injected with St-PGA-OG-mUNO (0.41 mg/0.5mL of PBS) or St-PGA-OG (0.35 mg/0.5mL

668 of PBS) (corresponding to 15nmoles of OG, fluorescence measured by UV-Vis). The homing
669 of a higher dose of St-PGA-PGA-mUNO (0.82 mg/0.5mL of PBS) or St-PGA-OG (0.7
670 mg/0.5mL of PBS) (corresponding to 30nmoles of OG) was also analysed and compared with
671 the homing of FAM-mUNO (30nmoles/0.5mL of PBS). In every case, nanoconjugates or free
672 peptide were circulated for 6 h, after which mice were sacrificed by anaesthetic overdose
673 followed by cervical dislocation. Organs and tumours were collected and fixed in cold 4% w/v
674 paraformaldehyde (PFA) in PBS at +4 °C for 24 h, washed in PBS at room temperature for 1
675 h and cryoprotected in 15% w/v sucrose (Sigma Life Science, cat. S9378) followed by 30%
676 w/v sucrose at 4 °C overnight. Cryoprotected and fixed tissues were frozen in OCT (Optimal
677 Cutting Temperature, Leica, cat. 14020108926), cryosectioned at 10 µm on Superfrost+ slides
678 (Thermo Fisher, cat. J1800AMNZ) and stored at -20 °C. Immunofluorescent staining was
679 performed as described earlier[42]. OG was detected using rabbit anti-FITC/Oregon Green
680 (dilution 1/100, Invitrogen by Thermo Fisher Scientific, cat. A889) and Alexa Fluor® 647 goat
681 anti-rabbit antibody (dilution 1/250, Invitrogen by Thermo Fisher Scientific, cat. A21245).
682 CD206 was detected using rat anti-mouse CD206 (dilution 1/150, Bio-Rad, cat. MCA2235GA)
683 and Alexa Fluor® 546 goat anti-rat antibody (dilution 1/250, life technologies, cat. A11081).
684 CD86 was detected using rat anti-mouse CD86 (dilution 1/100, BioLegend, cat. 105001) and
685 Alexa Fluor® 546 goat anti-rat secondary antibody (dilution 1/250). CD11c was detected using
686 hamster anti-mouse CD11c antibody (dilution 1/75, BioLegend, cat. 117301) and Alexa
687 Fluor® 546 goat anti-hamster secondary antibody (dilution 1/200, life technologies, cat.
688 A21111) Slides were counterstained using 4′,6-diamidino-2-phenylindole (DAPI, 1 µg/mL in
689 PBS, Sigma-Aldrich, cat. D9542-5MG). Coverslips were mounted using mounting medium
690 (Fluoromount-G™ Electron Microscopy Sciences, cat. 17984-25), and sections were imaged
691 using Zeiss confocal microscope (Zeiss LSM-710) and 20x objective. The colocalisation
692 analysis shown in Fig. 2M-P, between the FAM or OG channel and the CD206 channel was
693 carried out using the "Coloc2" plugin in the Fiji programme and selecting the "Pearson's R
694 value (no threshold)" coefficient. The colocalisation values were obtained from at least three
695 representative images per mouse per group and their average and standard error were plotted.
696 The OG/FAM mean signal per $CD206^+$ cell analysis was measured using the ImageJ
697 programme, taking the mean OG/FAM signal, and dividing it with the number of $CD206^+$ cells.
698 Average values were obtained from four images per mouse. N=3 for orthotopic TNBC and
699 N=2 for the homing in experimental metastasis of TNBC.
700

701 **Analysis of tumour and liver leakiness**

702 Endogenous IgG immunostaining of orthotopic 4T1 tumours and livers was performed
703 following the same IF protocol as described above to assess leakiness. Endogenous IgG was
704 detected using Alexa Fluor® 647 goat anti-mouse antibody (dilution 1/200, Invitrogen by
705 Thermo Fisher Scientific, cat. A21235) and slides were counterstained with DAPI (1 µg/mL in
706 PBS). The coverslips were mounted, and sections were imaged using Zeiss confocal
707 microscope and 20x objective (N=3 tumours).

708

709 **PDL1 expression analysis in orthotopic TNBC tumours**

710 The assessment of PDL1 expression in orthotopic 4T1 tumours followed the IF protocol
711 described above. PDL1 was detected using rat anti-mouse PDL1 (dilution 1/100, BioLegend,
712 cat. 124302) as primary antibody and Alexa Fluor® 647 goat anti-rat (dilution 1/200,
713 Invitrogen, cat. A21247) as the secondary antibody. Slides were counterstained with DAPI (1
714 µg/mL in PBS), mounted, and imaged using a Zeiss confocal microscope.

715

716 **Tumour homing of anti-PDL1 in orthotopic TNBC tumours**

717 For the homing analysis with anti-PDL1, we injected $1x10^6$ 4T1 cells in 50 µL of PBS s.c. and
718 ten days p.i., PDL1 antibody (5 mg/kg, rat anti-mouse, BioXcell, cat. BE0101) was injected
719 i.v., circulated for 24 h after which mice were sacrificed, organs collected and fixed with PFA.
720 Ten µm tissue sections were stained with Alexa Fluor® 647 goat anti-rat antibody (dilution
721 1/200), counterstained with DAPI (1 µg/mL in PBS), mounted, and imaged with a Zeiss
722 confocal microscope.

723

724 **Plasma half-life evaluation for St-PGA-OG-mUNO**

725 Plasma half-life studies were performed as previously described[42]. Briefly, healthy female
726 Balb/c mice (N=3) were i.p. injected with St-PGA-OG-mUNO (0.41 mg/0.5mL of PBS,
727 corresponding to 15nmoles OG). Ten µL of blood was sampled at different timepoints (0, 5,
728 10, 15, 30, 60, 180, 360, and 1440 min) and mixed with 50 µL of PBS-Heparin solution. Blood
729 samples were centrifuged to obtain plasma (300g for 5 min at room temperature) and OG
730 fluorescence was read with a plate reader (FlexStation II Molecular Devices) at 480nm
731 excitation/520nm emission.

732

733 **DOX release studies**

734 LC-MS was implemented to determine free drug levels, stability, and drug release with
735 OximUNO. The LC-MS system consisted of an ExionLC LC system and AB Sciex QTRAP
736 4500, a triple quadrupole ion trap hybrid equipped with a Turbo VTM electrospray ionisation
737 source. DOX was detected with an internal standard method: 1 µg/mL of daunorubicin (DAU)
738 was used as internal standard, where three calibration curves (in a range from 0.5 to 50 µg/mL
739 DOX) were prepared and used for accurate analysis of DOX in the samples. Both DOX and
740 DAU were detected with positive electrospray ionisation mode by following two mass
741 transitions (544.2 m/z → 397 m/z and 544.2 m/z → 379 m/z for DOX, and 528 m/z → 363.1
742 m/z and 528 m/z → 321.3 m/z for DAU). The obtained LC-MS optimal conditions were as
743 follows: flow rate 0.5 mL/min; mobile phase – 0.05 % trifluoroacetic acid with 70 % of
744 acetonitrile; LiChrospher 100 C18 column (125x4.0 mm) (Merck); column temperature 40 ºC,
745 10 µL injection volume.
746 Stability study of OximUNO conjugate in PBS, pH 7.4
747 OximUNO was incubated in 10 mM dPBS at 37 °C at the concentration of 3 mg/mL and with
748 3 µg/mL of DAU. 100 µL aliquots were collected at defined time points (0, 1, 2, 5, 24, 48, 72
749 h), extracted with 3x250 µL chloroform, and mixed by vortexing for 5 min. Organic phases
750 from all three chloroform extracts were collected in one tube, evaporated using speed vacuum,
751 and stored at -20 °C. On the day of analysis, dried samples were reconstituted in 300 µL of
752 methanol (LC-MS grade), vortexed for 5 min and centrifuged for 5 min at 30,437g.
753 Supernatants were filtered through a 0.45 µm filter and subjected to LC-MS analysis.
754 Stability study of OximUNO in the i.p. fluid
755 I.p. fluid was collected from healthy 8-12-week old Balb/c female mice as performed in REF[100]
756 by collecting the supernatant and discarding the pellet after the centrifugation step. A working
757 solution containing 3 mg/mL of OximUNO and 3 µg/mL of DAU in i.p. fluid was incubated
758 at 37 °C. 50 µL aliquots were collected at scheduled time points (0, 2, 5, 7, and 24 h). Samples
759 were then diluted with 100 µL of methanol, sonicated to dissolve DOX, and injected into the
760 LC-MS after filtration through a 0.45 µm filter.
761
762 Cathepsin B release kinetic studies.
763 Cathepsin B (5 IU) was activated in 2 mM EDTA, 5 mM DTT, and 20 mM CH_3COONa buffer
764 and incubated at 37 °C for 15 min. In a separate tube, a solution containing 3 mg/mL OximUNO
765 and 3 µg/mL of DAU was prepared with 20 mM CH_3COONa and incubated at 37 °C for 15
766 min. The two solutions were then combined to produce a reaction solution that was incubated

767 at 37 °C. 100 µL aliquots were collected at scheduled time points (0, 1, 2, 5, 8, 24, 48, 72 h),
768 and after the addition of 900 µL of dPBS (to adjust the pH level to 7.4), free DOX and DAU
769 were extracted with 2.5 mL of $CHCl_3$ three times. Samples were processed as described under
770 "Stability Study of OximUNO conjugate in PBS, pH 7.4". After $CHCl_3$ evaporation, samples
771 were reconstituted with 300 µL of methanol, filtered through a 0.45 µm filter and subjected to
772 LC-MS analysis. A blank solution was prepared with the same components as the sample
773 solution but without cathepsin B and used as a control sample.
774
775 **In vitro cytotoxicity assay**
776 Human peripheral blood mononuclear cells (PBMC) were purified from human blood buffy
777 coat using Ficoll Paque Plus (GE Healthcare, cat. 17-1440-02) reagent and $CD14^+$ microbeads
778 (MACS Miltenyi Biotec, cat. 130-050-201) as previously described[42]. $1.2x10^5$ cells in 50 µL
779 of RPMI-1640 medium were seeded on an FBS-coated 96-well plate. To obtain M0
780 macrophages, 50 µL of macrophage colony stimulating factor (M-CSF) (100 ng/mL,
781 BioLegend, cat. 574802) was added and replenished every other day for four days by
782 substituting the half of the medium with fresh medium containing M-CSF. To obtain optimal
783 macrophage attachment and M2 polarisation, 50 µL of interleukin-4 (IL-4, 50 ng/mL,
784 BioLegend, cat. 574002) and M-CSF (100 ng/mL) mixture was added to the wells. The medium
785 was replenished by substituting half of the medium with fresh medium containing IL-4 and M-
786 CSF every other day for six days. To obtain M1 macrophages, monocytes were incubated with
787 M-CSF (100 ng/mL) for six days, replenishing every other day with fresh medium containing
788 M-CSF and on day six, 50 µL of M-CSF, lipopolysaccharide (LPS, 100 ng/mL, Sigma Aldrich,
789 cat. L4391) and interferon-γ (IFN-γ, 20 ng/mL, BioLegend, cat. 570202) was added and
790 incubated overnight. On day seven for M2 and M1 macrophages or day four for M0
791 macrophages, cells were incubated for 15 min at 37 °C with OximUNO, St-PGA-DOX, DOX
792 in medium, or free medium as a control (N=3 wells per group). Concentrations used were
793 calculated based on DOX: 33µM and 100µM. (Of note, the dose of OximUNO used for the 33
794 µM DOX experiments shown in Figure 3E corresponds to the same dose of OximUNO used
795 for both in vivo treatment studies. In vivo, all treated groups received injections containing 2
796 mg/Kg DOX, which, assuming the dilution in mouse blood, corresponds to a DOX
797 concentration of 33 µM). After incubation, wells were washed, fresh medium added, and cells
798 incubated for 48 h at 37 °C. After 48 h, 10 µL of 3-(4,5-dimethylthiazol-2-yl)-2,5-
799 diphenyltetrazolium bromide (MTT, concentration 5 mg/mL, Invitrogen, cat. M6494) in PBS

800 was added to each well containing culture medium and incubated for 2.5 h at 37 °C. Medium
801 containing MTT was then removed without removing formed crystals, and 100 µL of
802 isopropanol was added to each well to dissolve crystals. Absorbance was read at 580 nm using
803 a plate reader (Tecan Sunrise) and the corresponding Magellan™ 7 programme.
804
805 **In vivo liver and kidney toxicology studies with OximUNO**
806 Three healthy 12-week-old female Balb/c mice were i.p. injected once with OximUNO (0.704
807 mg/0.5mL PBS or 1.408mg/0.5mL) and circulated for 48 h. Then, mice were anesthetised, and
808 blood collected through retro-orbital bleeding into Lithium Heparin tubes (BD Vacutainer, cat.
809 368494). Blood samples were centrifuged at 1800g for 15 min at +4 °C and 400 µL of plasma
810 was collected for analysis. Samples were analysed in Tartu University Hospital using a Cobas
811 6000 IT-MW (Roche Diagnostics Gmbh) machine and reagents for creatinine (CREP2, cat.
812 03263991) and alanine aminotransferase (ALTLP, cat. 04467388).
813
814 **OximUNO treatment of orthotopic TNBC**
815 $5x10^4$ 4T1 cells in 50 µL of PBS were s.c. injected into the fourth mammary fat pad of 8-12-
816 week-old female Balb/c mice. On day seven, mice were sorted into four groups by tumour
817 volume measured using a digital calliper (Mitutoyo). Tumour volume was calculated based on
818 the formula $(W^2 \times L)/2$, where W is the tumour's width and L is the tumour's length. The
819 starting volume for each group was ~25 mm^3, and the number of mice in each group was five.
820 The first i.p. injection of compounds was carried out on day seven, followed by an i.p. injection
821 every other day; nine injections were performed in total. The dose of nanoconjugates was
822 calculated based on DOX, 2mg/kg per injection (DOX: 39.5 µg/0.5mL PBS; St-PGA-DOX:
823 476 µg/0.5mL PBS; OximUNO: 341 µg/0.5mL PBS) giving a cumulative dose of DOX of 18
824 mg/kg. Mouse bodyweight and tumour volumes were monitored every other day. The final
825 injection was on day 25 and all mice were sacrificed on day 28. Tumour tissues were processed
826 as described under "In vivo biodistribution studies", and the lungs and hearts were embedded
827 in paraffin and processed for haematoxylin and eosin (H&E) staining (described below).
828 Tumours were immunostained as described above. CD206 was detected using rat anti-mouse
829 CD206 (dilution 1/200), CD8 using rat anti-mouse CD8 (dilution 1/75 Biolegend, cat. number
830 100701), FOXP3 using rat anti-mouse FOXP3 (dilution 1/75, Biolegend, cat number 126401)
831 as primary antibodies, Alexa Fluor® goat anti-rat 647 (dilution 1/300 for CD206 and 1/200 for
832 CD8, FOXP3,) was used as a secondary antibody for all markers. Slides were counterstained

833 with DAPI (1 μg/mL in PBS) and imaged using a Zeiss confocal microscope with a 10x
834 objective. All five tumours from each group were included in the IF analysis and at least three
835 images per mouse per group were included. Fluorescent signal intensity was calculated using
836 the ImageJ programme; to account for different amounts of tissue in the different images, only
837 the area containing tissue was selected and the "mean signal intensity" given by the programme
838 taken (total integrated intensity divided by the selected area). For this analysis, at least three
839 images per tumour were included.
840
841 **H&E staining in paraffin-embedded formalin-fixed tissues**
842 For H&E staining, 2 μm sections were cut from paraffin-embedded blocks. Slides were
843 warmed at 60 °C for 2 min before deparaffinising using xylene (3x2 min, 1x1 min) followed
844 by 100% ethanol washes (3x1 min), 80% ethanol wash (1x1 min) followed by 1 min wash in
845 water. Slides were first incubated with ST-1 HemaLast for 30 s, followed by ST-2
846 Haematoxylin for 5 min after which slides were washed in water for 2 min. Then, ST-3
847 Differentiator was added for 45 s, and slides were washed in water for 1 min. Next, ST-4 Bluing
848 Agent was added (1 min), washed for 1 min in water followed by 1 min incubation in 80%
849 ethanol, after which ST-5 Eosin was added and incubated for 1 min. For rehydration,
850 incubations in 100% ethanol (2x30 s, 1x2 min) were carried out and finished with incubations
851 in xylene (2x2 min). All washes were carried out in tap water. H&E stainings were performed
852 in Tartu University Hospital by pathologists using Leica staining automat and ST Infinity H&E
853 Staining System (Leica, cat. 38016998). Stained lung sections were scanned using a slide
854 scanner (Leica SCN400) and 20x zoom. Images were analysed using the QuPath programme
855 (version 0.1.2)[101]. Five levels ~1 mm apart were used for each mouse to obtain comprehensive
856 pulmonary metastases profile. Stained heart sections were also scanned using a slide scanner
857 and analysed with the QuPath programme. Tartu University Hospital pathologists assessed
858 cardiotoxicity in hearts and pulmonary metastases.
859
860 **Analysis of CD31 expression and blood vessel count**
861 CD31 expression after treating orthotopic TNBC tumours with OximUNO, St-PGA-DOX, or
862 DOX was detected using rat anti-mouse CD31 (dilution 1/100, BD Biosciences, cat. 553370)
863 and Alexa Fluor® 546 goat anti-rat (dilution 1/200, Invitrogen, cat. A11081) was used as the
864 secondary antibody. Slides were counterstained with DAPI (1 μg/mL in PBS) and imaged using
865 Zeiss confocal microscope with a 10x objective. CD31 expression was calculated using ImageJ

866 and mean signal per field as described under "OximUNO therapy in orthotopic TNBC",
867 including at least five images per mouse per group, N=5 mice per group. The blood vessel
868 count was calculated from the same images using ImageJ as follows: the image was changed
869 to an 8-bit image, threshold (Triangle algorithm with modifications to account for as much
870 actual CD31 signal as possible) was added, and particles analysed. At least three images per
871 mouse per group were included in the analysis, N=5 mice per group.
872
873 **OximUNO treatment of experimental metastasis of TNBC**
874 $2x10^5$ 4T1 cells in 100 µL of PBS were i.v. injected into the tail vein of 8-12-week-old female
875 Balb/c mice. Treatment with OximUNO, St-PGA-DOX, or DOX began on day four p.i.; each
876 group comprised six mice. Doses of different compounds were calculated based on DOX
877 (2mg/kg): DOX: 39.5 µg/0.5mL PBS; St-PGA-DOX: 774.5 µg/0.5mL PBS; OximUNO: 704
878 µg/0.5mL PBS. Mouse bodyweight was monitored every other day. A total of six injections
879 were carried out every other day. The final injection was on day 12, and all animals were
880 sacrificed on day 18 using anaesthetic overdose and perfusion with PBS. Three right lungs
881 from each group were analysed with flow cytometry (FC), and three full lungs and three left
882 lungs from each group were frozen into blocks using OCT. Frozen lung tissues were
883 cryosectioned as described earlier, fixed with cold 4% PFA (CD206) or acetone (for CD8 and
884 FOXP3), and stained as described in the following section. Immunofluorescent stainings were
885 performed using the same markers and antibodies as shown in the "OximUNO treatment in
886 orthotopic TNBC" section.
887
888 **GFP staining and imaging**
889 Six lungs from each group were frozen in OCT. Ten µm sections were cut, and slides were
890 kept at -20 °C until ready to use. Slides were taken out of the freezer at least 30 min before
891 staining. For staining, slides were fixed with 4% PFA for 10 min at room temperature, washed
892 with PBS for 10 min at room temperature, counterstained using DAPI (1 µg/mL in PBS) for 5
893 min at room temperature, washed 3x4 min with PBS and finally mounted using mounting
894 medium. Permeabilisation was not used in this step to improve GFP visualisation. GFP was
895 visualised using its native fluorescence. Slides were imaged using Olympus confocal
896 microscope (FV1200MPE) with a 10x objective.
897
898 **Macroscopic analysis of GFP Signal**

899 Lungs from each group were imaged using Illumatool Bright Light System LT-9900
900 (LightTool's Research) in the green channel to visualise the fluorescent signal
901 macroscopically, and a photograph of each lung was taken. The total GFP signal of each lung
902 was quantified using the ImageJ programme using the "IntDen" value.
903
904 **Flow cytometry analysis**
905 Three mice were sacrificed using anaesthetic overdose, perfused with PBS and right lung
906 tissues were placed in cold RPMI-1640 medium supplemented with 2% v/v FBS. Lungs were
907 cut into small pieces on ice in a solution containing collagenase IV (160 U/mL, Gibco
908 cat.17104019)/dispase (0.6 U/mL, Gibco, cat. 17105-041)/DNase I (15 U/mL; AppliChem, cat.
909 A3778) mixture. To obtain a single-cell suspension, lung pieces were incubated in 10 mL of
910 the same mixture at 37 °C on a rotating platform for 45-60 min, pipetting every 10 min to
911 improve digestion. The cells were washed with 5 mL of RB ("running buffer": 4 mL 0.5M
912 EDTA, 100 mL v/v FBS in 1L of PBS), centrifuged (350g, 7 min, 4 °C), and red blood cells
913 were lysed with 3 mL of ammonium-chloride-potassium lysing buffer (ACK) at room
914 temperature. Ten mL of RB was added, cells were centrifuged and filtered using a 100 µm cell
915 strainer (Falcon, cat. 352360). Cells were counted using the brightfield mode of LUNA™
916 Automated Cell counter (Logos Biosystems). Cells were collected in RB at a concentration of
917 $5x10^6$/100µL, placed on a 96-well plate with conical bottom and incubated for 30 min in FcR-
918 blocking 2.4G2 hybridoma medium at 4 °C. The cells were then stained for either macrophage
919 or T cell markers for 25-45 min in the dark at +4 °C, centrifuged and washed twice with RB.
920 The antibodies used are listed in Table 2. For intracellular staining of T cells, cells were fixed
921 using eBioscience™ FOXP3/Transcription Factor Staining Buffer Set (Thermo Fisher, cat. 00-
922 5523-00) according to the protocol provided. Cells were stained for 25-45 min in the dark at
923 room temperature following permeabilisation and washed twice using RB. All cells were
924 collected in 150 µL of RB, filtered through a 70 µm filter (Share Group Limited) and 150 µL
925 of RB was used to wash the filter. BD LSRFortessa Flow Cytometer and FCS Express 7 Flow
926 (De Novo Software) were used for analysis.
927
928
929
930 **Table 2. Antibodies used in FC analysis: macrophage and T cell markers.**

M	Antibody	Dilution, company

	PerCP/Cyanine5.5 anti-mouse CD206 (MMR)	1/200, BioLegend, clone C068C2, cat. 141715
	PE anti-mouse CD86	1/400, BioLegend, clone PO3, cat. 105105
	PE/Cyanine7 anti-mouse F4/80	1/200, BioLegend, clone BM8, cat. 123114
	PE/Dazzle™ 594 anti-mouse/human CD11b	1/ 800, BioLegend, clone M1/70, cat. 101255
	eBioscience™ Fixable Viability Due eFluor™ 506	1/800, Thermo Fisher Scientific, cat. 65-0866-18
T cell markers	Brilliant Violet 570™ anti-mouse CD4	1/400, BioLegend, clone RM4-5, cat. 100542
	Brilliant Violet 605™ anti-mouse CD8a	1/400, BioLegend, clone 53-6.7, cat. 100744
	PE/Dazzle™ 594 anti-mouse CD279 (PD-1)	1/200, BioLegend, clone 29F.1A12, cat. 135228
	Alexa Fluor® 488 anti-mouse FOXP3	1/100, BioLegend, clone MF-14, cat 126406
	PerCP/Cyanine5.5 anti-mouse CD3ε	1/200, BioLegend, clone 145-2C11, cat. 100328
	Brilliant Violet 421™ anti-mouse CD152 (CTLA4)	1/200, BioLegend, clone UC10-4B9, cat. 106312
	eBioscience™ Fixable Viability Due eFluor™ 506	1/800, Thermo Fisher Scientific, cat. 65-0866-18

H&E staining on PFA-fixed cryosections

Ten µm sections were cut from unfixed tissues in a frozen block; sections were stored at -20 °C until ready to use. When ready, slides were taken out of the freezer at least 30 min before staining. Room temperature slides were fixed with cold 4% PFA for 10 min at room temperature followed by washing in PBS for 10 min at room temperature. After washing, slides were dipped into Mayer's haematoxylin solution (see preparation under "Reagents and Solutions") for 10 s, followed by washing in running tap water for 5 min. Then, slides were dipped into Eosin (5%) solution (see preparation under "Reagents and Solutions") for 20 s, followed by washing in running tap water for 5 min. For rehydration, slides were placed first in 96% ethanol (2x2min) followed by 100% ethanol (2x2min). For clearance slides were placed in RotiClear® solution (Roth, cat. A538.5) for two-times 5 min, after which slides were mounted using Eukitt® quick-hardening mounting medium (Merck, cat. 03989). Slides were scanned using Leica DM6 B microscope and Leica Aperio Versa 8 slides scanner with 20x zoom and images were analysed using the ImageScope programme (version 12.3.3).

Statistical analysis

All statistical analysis was carried out using One-Way ANOVA and Fisher LSD tests, using the Statistica programme (release 7).

DATA AVAILABILITY

952 All data needed to evaluate the conclusions on the paper are presented in the paper and/or the
953 Supplementary Information. Additional data related to the findings of this study are available
954 from the corresponding authors.
955
956
957 # REFERENCES

958 1. Rivenbark, A. G., O'Connor, S. M. & Coleman, W. B. Molecular and cellular
959 heterogeneity in breast cancer: challenges for personalized medicine. *Am. J. Pathol.* **183**,
960 1113–1124 (2013).
961 2. Foulkes, W. D., Smith, I. E. & Reis-Filho, J. S. Triple-Negative Breast Cancer. *N. Engl. J.*
962 *Med.* **363**, 1938–1948 (2010).
963 3. Lehmann, B. D. *et al.* Identification of human triple-negative breast cancer subtypes and
964 preclinical models for selection of targeted therapies. *J. Clin. Invest.* **121**, 2750–2767
965 (2011).
966 4. Garrido-Castro, A. C., Lin, N. U. & Polyak, K. Insights into Molecular Classifications of
967 Triple-Negative Breast Cancer: Improving Patient Selection for Treatment. *Cancer*
968 *Discov.* **9**, 176–198 (2019).
969 5. Pardoll, D. M. The blockade of immune checkpoints in cancer immunotherapy. *Nat. Rev.*
970 *Cancer* **12**, 252–264 (2012).
971 6. Esfahani, K. *et al.* A Review of Cancer Immunotherapy: From the Past, to the Present, to
972 the Future. *Curr. Oncol.* **27**, 87–97 (2020).
973 7. Adams, S. *et al.* Current Landscape of Immunotherapy in Breast Cancer: A Review. *JAMA*
974 *Oncol.* **5**, 1205–1214 (2019).
975 8. Gong, J., Chehrazi-Raffle, A., Reddi, S. & Salgia, R. Development of PD-1 and PD-L1
976 inhibitors as a form of cancer immunotherapy: a comprehensive review of registration
977 trials and future considerations. *J. Immunother. Cancer* **6**, 8 (2018).

978 9. Schmid, P. *et al.* Atezolizumab and Nab-Paclitaxel in Advanced Triple-Negative Breast
979 Cancer. *N. Engl. J. Med.* **379**, 2108–2121 (2018).
980 10. Schmid, P. *et al.* Atezolizumab plus nab-paclitaxel as first-line treatment for
981 unresectable, locally advanced or metastatic triple-negative breast cancer (IMpassion130):
982 updated efficacy results from a randomised, double-blind, placebo-controlled, phase 3
983 trial. *Lancet Oncol.* **21**, 44–59 (2020).
984 11. Marra, A., Viale, G. & Curigliano, G. Recent advances in triple negative breast
985 cancer: the immunotherapy era. *BMC Med.* **17**, 90 (2019).
986 12. Mori, H. *et al.* The combination of PD-L1 expression and decreased tumor-infiltrating
987 lymphocytes is associated with a poor prognosis in triple-negative breast cancer.
988 *Oncotarget* **8**, 15584–15592 (2017).
989 13. Mittendorf, E. A. *et al.* PD-L1 Expression in Triple-Negative Breast Cancer. *Cancer*
990 *Immunol. Res.* **2**, 361–370 (2014).
991 14. Socinski, M. A. *et al.* Atezolizumab for First-Line Treatment of Metastatic
992 Nonsquamous NSCLC. *N. Engl. J. Med.* **378**, 2288–2301 (2018).
993 15. Adams, S. *et al.* Patient-reported outcomes from the phase III IMpassion130 trial of
994 atezolizumab plus nab-paclitaxel in metastatic triple-negative breast cancer. *Ann. Oncol.*
995 **31**, 582–589 (2020).
996 16. Fecher, L. A., Agarwala, S. S., Hodi, F. S. & Weber, J. S. Ipilimumab and Its
997 Toxicities: A Multidisciplinary Approach. *The Oncologist* **18**, 733–743 (2013).
998 17. Hunter, G., Voll, C. & Robinson, C. A. Autoimmune inflammatory myopathy after
999 treatment with ipilimumab. *Can. J. Neurol. Sci. J. Can. Sci. Neurol.* **36**, 518–520 (2009).
1000 18. Maker, A. V. *et al.* Tumor Regression and Autoimmunity in Patients Treated With
1001 Cytotoxic T Lymphocyte–Associated Antigen 4 Blockade and Interleukin 2: A Phase I/II
1002 Study. *Ann. Surg. Oncol.* **12**, 1005–1016 (2005).

1003 19. Phan, G. Q. *et al.* Cancer regression and autoimmunity induced by cytotoxic T
1004 lymphocyte-associated antigen 4 blockade in patients with metastatic melanoma. *Proc.*
1005 *Natl. Acad. Sci. U. S. A.* **100**, 8372–8377 (2003).
1006 20. Cretella, D. *et al.* Pre-treatment with the CDK4/6 inhibitor palbociclib improves the
1007 efficacy of paclitaxel in TNBC cells. *Sci. Rep.* **9**, 13014 (2019).
1008 21. Arola, O. J. *et al.* Acute Doxorubicin Cardiotoxicity Involves Cardiomyocyte
1009 Apoptosis. *Cancer Res.* **60**, 1789–1792 (2000).
1010 22. Zhang, S. *et al.* Identification of the molecular basis of doxorubicin-induced
1011 cardiotoxicity. *Nat. Med.* **18**, 1639–1642 (2012).
1012 23. Keklikoglou, I. *et al.* Chemotherapy elicits pro-metastatic extracellular vesicles in
1013 breast cancer models. *Nat. Cell Biol.* **21**, 190–202 (2019).
1014 24. Hughes, R. *et al.* Perivascular M2 Macrophages Stimulate Tumor Relapse after
1015 Chemotherapy. *Cancer Res.* **75**, 3479–3491 (2015).
1016 25. Lewis, C. E. & Pollard, J. W. Distinct Role of Macrophages in Different Tumor
1017 Microenvironments. *Cancer Res.* **66**, 605–612 (2006).
1018 26. Peranzoni, E. *et al.* Macrophages impede CD8 T cells from reaching tumor cells and
1019 limit the efficacy of anti–PD-1 treatment. *Proc. Natl. Acad. Sci.* **115**, E4041–E4050
1020 (2018).
1021 27. Neubert, N. J. *et al.* T cell–induced CSF1 promotes melanoma resistance to PD1
1022 blockade. *Sci. Transl. Med.* **10**, eaan3311 (2018).
1023 28. Daurkin, I. *et al.* Tumor-Associated Macrophages Mediate Immunosuppression in the
1024 Renal Cancer Microenvironment by Activating the 15-Lipoxygenase-2 Pathway. *Cancer*
1025 *Res.* **71**, 6400–6409 (2011).

1026 29. Gok Yavuz, B. *et al.* Cancer associated fibroblasts sculpt tumour microenvironment
1027 by recruiting monocytes and inducing immunosuppressive PD-1+ TAMs. *Sci. Rep.* **9**, 3172
1028 (2019).
1029 30. Pathria, P., Louis, T. L. & Varner, J. A. Targeting Tumor-Associated Macrophages in
1030 Cancer. *Trends Immunol.* **40**, 310–327 (2019).
1031 31. DeNardo, D. G. *et al.* Leukocyte Complexity Predicts Breast Cancer Survival and
1032 Functionally Regulates Response to Chemotherapy. *Cancer Discov.* **1**, 54–67 (2011).
1033 32. Mancini, V. S. B. W., Pasquini, J. M., Correale, J. D. & Pasquini, L. A. Microglial
1034 modulation through colony-stimulating factor-1 receptor inhibition attenuates
1035 demyelination. *Glia* **67**, 291–308 (2019).
1036 33. Lee, S., Shi, X. Q., Fan, A., West, B. & Zhang, J. Targeting macrophage and
1037 microglia activation with colony stimulating factor 1 receptor inhibitor is an effective
1038 strategy to treat injury-triggered neuropathic pain. *Mol. Pain* **14**, 1744806918764979
1039 (2018).
1040 34. Bissinger, S. *et al.* Macrophage depletion induces edema through release of matrix-
1041 degrading proteases and proteoglycan deposition. *Sci. Transl. Med.* **13**, eabd4550 (2021).
1042 35. Wesolowski, R. *et al.* Phase Ib study of the combination of pexidartinib (PLX3397), a
1043 CSF-1R inhibitor, and paclitaxel in patients with advanced solid tumors. *Ther. Adv. Med.*
1044 *Oncol.* **11**, 1758835919854238 (2019).
1045 36. Papadopoulos, K. P. *et al.* First-in-Human Study of AMG 820, a Monoclonal Anti-
1046 Colony-Stimulating Factor 1 Receptor Antibody, in Patients with Advanced Solid Tumors.
1047 *Clin. Cancer Res.* **23**, 5703–5710 (2017).
1048 37. Kitamura, T. *et al.* Monocytes Differentiate to Immune Suppressive Precursors of
1049 Metastasis-Associated Macrophages in Mouse Models of Metastatic Breast Cancer. *Front.*
1050 *Immunol.* **8**, (2018).

1051 38. Madsen, D. H. *et al.* Tumor-Associated Macrophages Derived from Circulating
1052 Inflammatory Monocytes Degrade Collagen through Cellular Uptake. *Cell Rep.* **21**, 3662–
1053 3671 (2017).
1054 39. Ishihara, D. *et al.* Wiskott-Aldrich Syndrome Protein Regulates Leukocyte-Dependent
1055 Breast Cancer Metastasis. *Cell Rep.* **4**, 429–436 (2013).
1056 40. Karousou, E. *et al.* Collagen VI and Hyaluronan: The Common Role in Breast
1057 Cancer. *BioMed Res. Int.* **2014**, 1–10 (2014).
1058 41. Scodeller, P. *et al.* Precision Targeting of Tumor Macrophages with a CD206 Binding
1059 Peptide. *Sci. Rep.* **7**, 14655 (2017).
1060 42. Lepland, A. *et al.* Targeting Pro-Tumoral Macrophages in Early Primary and
1061 Metastatic Breast Tumors with the CD206-Binding mUNO Peptide. *Mol. Pharm.* **17**,
1062 2518–2531 (2020).
1063 43. Asciutto, E. K. *et al.* Phage-Display-Derived Peptide Binds to Human CD206 and
1064 Modeling Reveals a New Binding Site on the Receptor. *J. Phys. Chem. B* **123**, 1973–1982
1065 (2019).
1066 44. Figueiredo, P. *et al.* Peptide-guided resiquimod-loaded lignin nanoparticles convert
1067 tumor-associated macrophages from M2 to M1 phenotype for enhanced chemotherapy.
1068 *Acta Biomater.* **133**, 231–243 (2021).
1069 45. Jameson, B. *et al.* Expression of DC-SIGN by Dendritic Cells of Intestinal and
1070 Genital Mucosae in Humans and Rhesus Macaques. *J. Virol.* **76**, 1866–1875 (2002).
1071 46. Conniot, J. *et al.* Immunization with mannosylated nanovaccines and inhibition of the
1072 immune-suppressing microenvironment sensitizes melanoma to immune checkpoint
1073 modulators. *Nat. Nanotechnol.* **14**, 891–901 (2019).

1074 47. Duro-Castano, A. *et al.* Well-Defined Star-Shaped Polyglutamates with Improved
1075 Pharmacokinetic Profiles As Excellent Candidates for Biomedical Applications. *Mol.*
1076 *Pharm.* **12**, 3639–3649 (2015).
1077 48. Arroyo-Crespo, J. J. *et al.* Tumor microenvironment-targeted poly-L-glutamic acid-
1078 based combination conjugate for enhanced triple negative breast cancer treatment.
1079 *Biomaterials* **186**, 8–21 (2018).
1080 49. Duro-Castano, A. *et al.* Polyglutamic acid-based crosslinked doxorubicin nanogels as
1081 an anti-metastatic treatment for triple negative breast cancer. *J. Controlled Release* **332**,
1082 10–20 (2021).
1083 50. Arroyo-Crespo, J. J. *et al.* Anticancer Activity Driven by Drug Linker Modification in
1084 a Polyglutamic Acid-Based Combination-Drug Conjugate. *Adv. Funct. Mater.* **28**,
1085 1800931 (2018).
1086 51. Shaffer, S. A. *et al.* In vitro and in vivo metabolism of paclitaxel poliglumex:
1087 identification of metabolites and active proteases. *Cancer Chemother. Pharmacol.* **59**,
1088 537–548 (2007).
1089 52. Gordon, S. R. *et al.* PD-1 expression by tumour-associated macrophages inhibits
1090 phagocytosis and tumour immunity. *Nature* **545**, 495–499 (2017).
1091 53. Zhang, M. *et al.* Anti-CD47 Treatment Stimulates Phagocytosis of Glioblastoma by
1092 M1 and M2 Polarized Macrophages and Promotes M1 Polarized Macrophages In Vivo.
1093 *PLOS ONE* **11**, e0153550 (2016).
1094 54. Simon-Gracia, L. *et al.* Bifunctional Therapeutic Peptides for Targeting Malignant B
1095 Cells and Hepatocytes: Proof of Concept in Chronic Lymphocytic Leukemia. *Adv. Ther.* **3**,
1096 2000131 (2020).

1097 55. MPD: Phenotype strain survey measures: alanine aminotransferase.
1098 https://phenome.jax.org/search/details/ssmeasures?searchterm=alanine+aminotransferase+
1099 &ontavail=2.
1100 56. BALB/c Mouse | Charles River Laboratories. https://www.criver.com/products-
1101 services/find-model/balbc-mouse?region=3616.
1102 57. Cassetta, L. & Kitamura, T. Targeting Tumor-Associated Macrophages as a Potential
1103 Strategy to Enhance the Response to Immune Checkpoint Inhibitors. *Front. Cell Dev. Biol.*
1104 **0**, (2018).
1105 58. Santoni, M. *et al.* Triple negative breast cancer: Key role of Tumor-Associated
1106 Macrophages in regulating the activity of anti-PD-1/PD-L1 agents. *Biochim. Biophys. Acta*
1107 *BBA - Rev. Cancer* **1869**, 78–84 (2018).
1108 59. Rodell, C. B. *et al.* TLR7/8-agonist-loaded nanoparticles promote the polarization of
1109 tumour-associated macrophages to enhance cancer immunotherapy. *Nat. Biomed. Eng.* **2**,
1110 578–588 (2018).
1111 60. Loeuillard, E. *et al.* Targeting tumor-associated macrophages and granulocytic
1112 myeloid-derived suppressor cells augments PD-1 blockade in cholangiocarcinoma. *J. Clin.*
1113 *Invest.* **130**, 5380–5396 (2020).
1114 61. Choo, Y. W. *et al.* M1 Macrophage-Derived Nanovesicles Potentiate the Anticancer
1115 Efficacy of Immune Checkpoint Inhibitors. *ACS Nano* **12**, 8977–8993 (2018).
1116 62. Arlauckas, S. P. *et al.* Arg1 expression defines immunosuppressive subsets of tumor-
1117 associated macrophages. *Theranostics* **8**, 5842–5854 (2018).
1118 63. Landry, A. P., Balas, M., Alli, S., Spears, J. & Zador, Z. Distinct regional ontogeny
1119 and activation of tumor associated macrophages in human glioblastoma. *Sci. Rep.* **10**,
1120 19542 (2020).

1121 64. Zheng, X. *et al.* Spatial Density and Distribution of Tumor-Associated Macrophages
1122 Predict Survival in Non–Small Cell Lung Carcinoma. *Cancer Res.* **80**, 4414–4425 (2020).
1123 65. Etzerodt, A. *et al.* Specific targeting of CD163+ TAMs mobilizes inflammatory
1124 monocytes and promotes T cell–mediated tumor regression. *J. Exp. Med.* **216**, 2394–2411
1125 (2019).
1126 66. Puig-Kröger, A. *et al.* Folate Receptor β Is Expressed by Tumor-Associated
1127 Macrophages and Constitutes a Marker for M2 Anti-inflammatory/Regulatory
1128 Macrophages. *Cancer Res.* **69**, 9395–9403 (2009).
1129 67. Viitala, M. *et al.* Immunotherapeutic Blockade of Macrophage Clever-1 Reactivates
1130 the $CD8^+$ T-cell Response against Immunosuppressive Tumors. *Clin. Cancer Res.* **25**,
1131 3289–3303 (2019).
1132 68. Linde, N. *et al.* Macrophages orchestrate breast cancer early dissemination and
1133 metastasis. *Nat. Commun.* **9**, 1–14 (2018).
1134 69. Witschen, P. M. *et al.* Tumor Cell Associated Hyaluronan-CD44 Signaling Promotes
1135 Pro-Tumor Inflammation in Breast Cancer. *Cancers* **12**, 1325 (2020).
1136 70. Guo, C. *et al.* Liposomal Nanoparticles Carrying anti-IL6R Antibody to the Tumour
1137 Microenvironment Inhibit Metastasis in Two Molecular Subtypes of Breast Cancer Mouse
1138 Models. *Theranostics* **7**, 775–788 (2017).
1139 71. Movahedi, K. *et al.* Nanobody-Based Targeting of the Macrophage Mannose
1140 Receptor for Effective *In Vivo* Imaging of Tumor-Associated Macrophages. *Cancer Res.*
1141 **72**, 4165–4177 (2012).
1142 72. Azad, A. K. *et al.* γ-Tilmanocept, a New Radiopharmaceutical Tracer for Cancer
1143 Sentinel Lymph Nodes, Binds to the Mannose Receptor (CD206). *J. Immunol.* **195**, 2019–
1144 2029 (2015).

1145 73. Jaynes, J. M., Lopez, H. W., Martin, G. R., YATES, C. & Garvin, C. E. Peptides
1146 having anti-inflammatory properties. (2016).
1147 74. Scodeller, P. & Asciutto, E. K. Targeting Tumors Using Peptides. *Molecules* **25**, 808
1148 (2020).
1149 75. Ekladious, I., Colson, Y. L. & Grinstaff, M. W. Polymer–drug conjugate therapeutics:
1150 advances, insights and prospects. *Nat. Rev. Drug Discov.* **18**, 273–294 (2019).
1151 76. Duro-Castano, A., Conejos-Sánchez, I. & Vicent, M. J. Peptide-Based Polymer
1152 Therapeutics. *Polymers* **6**, 515–551 (2014).
1153 77. Moura, L. I. F. *et al.* Functionalized branched polymers: promising
1154 immunomodulatory tools for the treatment of cancer and immune disorders. *Mater. Horiz.*
1155 **6**, 1956–1973 (2019).
1156 78. Melnyk, T., Đorđević, S., Conejos-Sánchez, I. & Vicent, M. J. Therapeutic potential
1157 of polypeptide-based conjugates: Rational design and analytical tools that can boost
1158 clinical translation. *Adv. Drug Deliv. Rev.* **160**, 136–169 (2020).
1159 79. Duro-Castano, A. *et al.* Capturing "Extraordinary" Soft-Assembled Charge-Like
1160 Polypeptides as a Strategy for Nanocarrier Design. *Adv. Mater.* **29**, 1702888 (2017).
1161 80. Duro-Castano, A., Movellan, J. & Vicent, M. J. Smart branched polymer drug
1162 conjugates as nano-sized drug delivery systems. *Biomater. Sci.* **3**, 1321–1334 (2015).
1163 81. Cortez-Retamozo, V. *et al.* Origins of tumor-associated macrophages and neutrophils.
1164 *Proc. Natl. Acad. Sci.* **109**, 2491–2496 (2012).
1165 82. Kurashige, M. *et al.* Origin of cancer-associated fibroblasts and tumor-associated
1166 macrophages in humans after sex-mismatched bone marrow transplantation. *Commun.*
1167 *Biol.* **1**, 1–13 (2018).
1168 83. Veglia, F. & Gabrilovich, D. I. Dendritic cells in cancer: the role revisited. *Curr.*
1169 *Opin. Immunol.* **45**, 43–51 (2017).

1170 84. Agostinis, P. *et al.* PHOTODYNAMIC THERAPY OF CANCER: AN UPDATE.
1171 *CA. Cancer J. Clin.* **61**, 250–281 (2011).
1172 85. Cheah, H. Y. *et al.* Near-Infrared Activatable Phthalocyanine–Poly-L-Glutamic Acid
1173 Conjugate: Enhanced in Vivo Safety and Antitumor Efficacy toward an Effective
1174 Photodynamic Cancer Therapy. *Mol. Pharm.* **15**, 2594–2605 (2018).
1175 86. Nguyen, V.-N., Yan, Y., Zhao, J. & Yoon, J. Heavy-Atom-Free Photosensitizers:
1176 From Molecular Design to Applications in the Photodynamic Therapy of Cancer. *Acc.*
1177 *Chem. Res.* **54**, 207–220 (2021).
1178 87. Tacar, O., Sriamornsak, P. & Dass, C. R. Doxorubicin: an update on anticancer
1179 molecular action, toxicity and novel drug delivery systems. *J. Pharm. Pharmacol.* **65**,
1180 157–170 (2013).
1181 88. Shan, H., Dou, W., Zhang, Y. & Qi, M. Targeted ferritin nanoparticle encapsulating
1182 CpG oligodeoxynucleotides induces tumor-associated macrophage M2 phenotype
1183 polarization into M1 phenotype and inhibits tumor growth. *Nanoscale* **12**, 22268–22280
1184 (2020).
1185 89. Ramesh, A., Brouillard, A., Kumar, S., Nandi, D. & Kulkarni, A. Dual inhibition of
1186 CSF1R and MAPK pathways using supramolecular nanoparticles enhances macrophage
1187 immunotherapy. *Biomaterials* **227**, 119559 (2020).
1188 90. Hollmén, M. *et al.* G-CSF regulates macrophage phenotype and associates with poor
1189 overall survival in human triple-negative breast cancer. *OncoImmunology* **5**, e1115177
1190 (2016).
1191 91. Georgoudaki, A.-M. *et al.* Reprogramming Tumor-Associated Macrophages by
1192 Antibody Targeting Inhibits Cancer Progression and Metastasis. *Cell Rep.* **15**, 2000–2011
1193 (2016).

1194 92. Zhang, F. *et al.* Reprogramming of profibrotic macrophages for treatment of
1195 bleomycin-induced pulmonary fibrosis. *EMBO Mol. Med.* **12**, e12034 (2020).
1196 93. Sartor, O. *et al.* Lutetium-177–PSMA-617 for Metastatic Castration-Resistant
1197 Prostate Cancer. *N. Engl. J. Med.* **0**, null (2021).
1198 94. Vikas, P., Borcherding, N. & Zhang, W. The clinical promise of immunotherapy in
1199 triple-negative breast cancer. *Cancer Manag. Res.* **10**, 6823–6833 (2018).
1200 95. Tian, C. *et al.* ff19SB: Amino-Acid-Specific Protein Backbone Parameters Trained
1201 against Quantum Mechanics Energy Surfaces in Solution. *J. Chem. Theory Comput.* **16**,
1202 528–552 (2020).
1203 96. AmberTools - SBGrid Consortium - Supported Software.
1204 https://sbgrid.org/software/titles/ambertools.
1205 97. Hopkins, C. W., Le Grand, S., Walker, R. C. & Roitberg, A. E. Long-Time-Step
1206 Molecular Dynamics through Hydrogen Mass Repartitioning. *J. Chem. Theory Comput.*
1207 **11**, 1864–1874 (2015).
1208 98. Berendsen, H. J. C., Postma, J. P. M., van Gunsteren, W. F., DiNola, A. & Haak, J. R.
1209 Molecular dynamics with coupling to an external bath. *J. Chem. Phys.* **81**, 3684–3690
1210 (1984).
1211 99. Ryckaert, J.-P., Ciccotti, G. & Berendsen, H. J. C. Numerical integration of the
1212 cartesian equations of motion of a system with constraints: molecular dynamics of n-
1213 alkanes. *J. Comput. Phys.* **23**, 327–341 (1977).
1214 100. Ray, A. & Dittel, B. N. Isolation of Mouse Peritoneal Cavity Cells. *J. Vis. Exp. JoVE*
1215 1488 (2010) doi:10.3791/1488.
1216 101. Bankhead, P. *et al.* QuPath: Open source software for digital pathology image
1217 analysis. *Sci. Rep.* **7**, 16878 (2017).
1218

ACKNOWLEDGEMENTS

We would like to thank Stuart P. Atkinson for English editing, Merje Jakobson for performing H&E studies on paraffin-embedded formalin-fixed tissues, Dr. Aivar Orav for in vivo toxicity study analysis and Dr. Mario Plaas for the help with the slide scanner. PS acknowledges support from the Estonian Research Council (grant: PUT PSG38 to PS) and a Feasibility fund of the University of Tartu (grant: ARENG51 to PS). AL acknowledges a PhD fellowship from the Estonian government. MJV acknowledges the support by European Research Council grants (ERC-CoG-2014-648831 "My-Nano" and ERC-PoC-2018-825798 "Polymmune"). Part of the equipment employed in this work has been funded by Generalitat Valenciana and co-financed with FEDER funds (PO FEDER of Comunitat Valenciana 2014–2020). UH acknowledges the support by EsRC Mobilitas+ grant MOBTP185. TT acknowledges the support by UT EIK grant and GMVBS0230PR.

AUTHOR CONTRIBUTIONS

AL performed the in vitro and in vivo experiments, histology, immunofluorescence, flow cytometry, analysis and wrote the manuscript. AM performed chemical design, synthesis, and characterisation and edited the manuscript. UH performed flow cytometry experiments and analysis. EA, MP, and MB performed computational simulations. SD performed drug release studies and chemical characterisation. LS performed analysis and expert evaluation of H&E images. PP edited the manuscript and provided discussions and lab support. TT edited the manuscript, participated in the experimental design and discussions, and provided laboratory support. MJV performed chemical design, in vitro and in vivo experiment design, supervised chemical synthesis and characterisation, provided lab support, and edited the manuscript. PS supervised all the experiments, participated in their design and analysis, and edited the manuscript. All authors edited the manuscript and approved the final version.

CORRESPONDING AUTHORS

Correspondence to Tambet Teesalu, María J. Vicent and Pablo Scodeller.

ETHICS DECLARATIONS

COMPETING INTERESTS

PS and TT are inventors of patents on the mUNO peptide. MJV is an inventor of a patent on BTA-core branched polypeptides (including St-PGA) licensed to PTS SL. In addition, TT is

1252 an inventor of iRGD and CendR peptides and a shareholder of Cend Therapeutics Inc., a
1253 company that holds a license for the mUNO, iRGD and CendR peptides.
1254
1255
1256 **FOR TABLE OF CONTENTS ONLY**

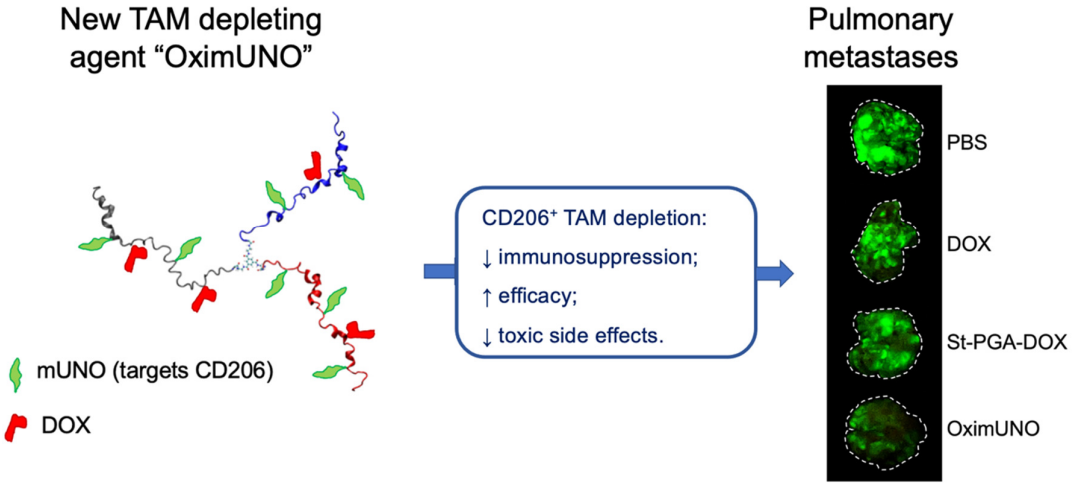

1257